Computers and Fluids 136 (2016) 402–420

Contents lists available at ScienceDirect

Computers and Fluids

journal homepage: www.elsevier.com/locate/compfluid

A robust interface method for drop formation and breakup simulation at high density ratio using an extrapolated liquid velocity

F. Xiao[a,b], M. Dianat[a], J.J. McGuirk[a,*]

[a] Department of Aeronautical and Automotive Engineering, Loughborough University, Loughborough LE11 3TU, UK
[b] Science and Technology on Scramjet Laboratory, College of Aerospace Science and Engineering, National University of Defense Technology, Changsha, 410073, China

ARTICLE INFO

Article history:
Received 16 April 2015
Revised 29 April 2016
Accepted 25 June 2016
Available online 27 June 2016

Keywords:
Extrapolated liquid velocity
Divergence free algorithm
Droplet breakup
Rayleigh-Taylor instability
High density ratio
Coupled level set/volume of fluid

ABSTRACT

A two-phase flow formulation for atomisation modelling is presented, with a Coupled Level Set/Volume Of Fluid (CLSVOF) technique adopted for interface-tracking. In order to achieve stable numerical solution at high density ratios, an extrapolated liquid velocity field is constructed and used in discretisation of the momentum equations. Solution accuracy is also improved when this field is also used in the scalar (VOF and Level Set) advection equations. A divergence-free algorithm is proposed to ensure satisfaction of the continuity condition for the extrapolated liquid velocity. The density and viscosity across the interface are treated sharply as a function of the Level Set to maintain the physical discontinuity. The developed method is shown to accurately predict drop formation in low Re liquid jets and the deformation and breakup morphology of a single droplet in uniform air flow at different Weber numbers (from 3.4 to 96). The mechanism for droplet breakup is determined based on an analysis of the simulation results. The computed Rayleigh–Taylor instability wavelength extracted from the acceleration of the simulated liquid droplet agrees well with experimental measurements and theoretical analysis, confirming that Rayleigh–Taylor instability dominates single drop breakup in the Weber number range studied. Finally, the influence of liquid viscosity on droplet breakup is numerically investigated; the critical Weber number separating deformation and breakup regimes is well predicted at different Ohnesorge numbers in comparison with the experimental data.

1. Introduction

An accurate method for atomisation prediction is of utmost significance in many industrial applications. Substantial research has therefore been carried out to understand the atomisation process. State of the art reviews relevant to this important phenomenon have appeared recently, for example [1] and [2]. These reviews have outlined the complex numerical challenges introduced by the need to deal with accurate liquid/gas interface tracking, discontinuous fluid properties across the interface, and surface tension effects.

Three popular interface capturing methods have been proposed for flows involving a liquid/gas interface. The first was the Volume of Fluid (VOF) method, where the VOF function F is defined as the liquid volume fraction within any element of space. It was first proposed by Hirt and Nichols [3], and further developed/applied in [4–13]. VOF can inherently conserve the liquid volume, but it needs significant numerical effort to extract the interface geometrical properties (normal and curvature) to 2nd order accuracy from F due to its discontinuous nature, especially in 3D [8,11,13,14]. An alternative choice for interface tracking, proposed by Sussman et al. [15], is the Level Set (LS) method, with recent developments reported in [16–18]. Unlike F the LS function ϕ is a continuous variable; the interface is defined by the contour $\phi = 0$, and ϕ represents the signed distance from the interface, with $\phi > 0$ liquid and $\phi < 0$ gas. The LS method thus provides a numerically more convenient representation of the interface, making it straightforward to locate interface position and calculate interface normal and curvature. However, the LS method can induce considerable error of liquid mass as the calculation advances in time [19], requiring special procedures to alleviate this problem [20–22]. To combine the advantages of VOF and LS methods into a single algorithm, a hybrid or coupled LS and VOF method (CLSVOF) has been proposed by Sussman and Puckett [23], with applications to two-phase flow simulations in [24–26].

* Corresponding author.
E-mail addresses: xiaof03@aliyun.com (F. Xiao), j.j.mcguirk@lboro.ac.uk (J.J. McGuirk).

http://dx.doi.org/10.1016/j.compfluid.2016.06.021

Simulation of atomisation at high liquid/gas density ratios is very challenging as it is prone to numerical instabilities [2,27]. Since the non-conservative form of the governing equations are commonly solved for incompressible two-phase flows, large momentum discretisation errors can occur in computational cells in the interface vicinity when cell face flux interpolations are carried out. Momentum flux interpolation is not straightforward near an interface since both density and velocity gradient (due to the viscosity discontinuity) change sharply; conventional linear interpolation practices can lead to significant errors that cause numerical instability as the density ratio increases. Rudmann [28], Raessi [29], and Desjardins and Moureau [30] describe various techniques to solve this problem, in particular special interpolation practices for cell face density are suggested. It would be preferable if the sharp jump in density (and viscosity) across the interface were retained as far as possible, so a more promising method has been proposed by Sussman et al. [24]; this introduces the concept of an extra liquid velocity field 'extrapolated' onto the gas phase side of the interface, and a modified version of this is incorporated in the present methodology.

Since it is computationally extremely expensive to carry out Direct Numerical Simulation of atomisation, a lot of effort has been put into the development of two-phase Large Eddy Simulation (LES). Additional complexities arise when applied to two-phase flows in connection with extra terms requiring sub-grid-scale (SGS) modelling. The surface tension term in the momentum equations is non-linear and hence filtering will lead to an additional SGS term; similarly, extra SGS fluxes will also appear due to the non-linear convection terms in the scalar equations which determine the interface behaviour (VOF and Level Set). In the vast majority of LES studies for two-phase flows so far, all specific SGS terms associated with the presence of an interface have been ignored, and this has been described by Gorokhovski and Herrmann [1] and Bianchi et al. [10] as quasi-DNS/LES as explained in the next section, this corresponds to an under-resolved DNS of interface tracking combined with an LES of the two-phase flow equations without any explicit inclusion of SGS surface tension modelling.

Different modelling approaches have been put forward in the last few years to address the extra SGS terms. The work of Toutant et al. [31,32] for example proposes a fundamentally different filtering approach for two-phase flows. This aims to account for the inevitable under-resolution of the interface in an LES calculation and leads to extra SGS terms modelled using a scale similarity principle. So far, however, this approach has only been analysed via explicit filtering of an a-priori DNS calculation to extract the extra terms introduced after LES filtering and compare these with proposed models; so far no actual LES calculations have been reported following this approach.

An alternative approach specifically relevant to surface tension SGS modelling has been proposed by Herrmann and Gorokhovski [33,34] and was recently investigated by Aniszewski et al. [35]. Calculation of the modelled surface tension SGS term requires evaluation of an expression which involves not only the filtered (resolved) surface normal $\overline{n}_i$, but also the instantaneous surface normal n_i. To calculate n_i requires the transport equations for the instantaneous interface-determining variables (F and ϕ) to be solved using the instantaneous velocity field. To reconstruct this from the LES-filtered velocity field the Approximate Deconvolution Model (ADM) of Stolz et al. [36] was used. The test cases used in [35] to assess the importance of the surface tension SGS term and the accuracy of the proposed model had low density ratios ($\leq$ 10), far removed from the typical (water/air) level of 800 of interest in the current work. Thus, it seems that SGS modelling fully extended to two-phase flow is still in its infancy, and, for this reason, the approach adopted in the present study was the quasi-DNS/LES approach.

In order to elucidate the physical atomisation mechanism, many experimental and numerical studies on the deformation/breakup of a single drop (often referred to as secondary atomisation) have been carried out [37]. The Weber number ($We = \rho_G U_G^2 D_0/\sigma$) which represents the ratio of the disintegrating aerodynamic force to the stabilising surface tension force is the most important characteristic parameter in single drop breakup. As We increases, several modes of behaviour are observed experimentally: a pure deformation mode, bag breakup, bag-stamen breakup, multimode breakup, sheet-thinning (or shear) breakup and shear-induced entrainment (or catastrophic breakup) [26,37–39]. Theofanous et al. [40] and Zhao et al. [41] demonstrated that the Rayleigh–Taylor instability determines the drop breakup morphology at low Weber number ($We < 80$) by comparing their theory with their own experimental results. The mechanism for droplet breakup has been more disputed for We higher than 80. The shear-stripping mechanism was proposed by Ranger and Nicholls [42] and was widely adopted in the last century [38]. In the shear-stripping mechanism, it is postulated that a liquid boundary layer is developed adjacent to the interface inside the drop under the action of shear stress from the gas flow. As the liquid boundary layer becomes unstable, liquid mass is stripped at the drop periphery. A lot of doubt has been cast on this shear-stripping mechanism by Liu and Reitz [43], Lee and Reitz [44], Guildenbecher et al. [37] and Theofanous et al. [39] [45]. The shear-stripping model suggests that the breakup mode should be a function of Re, which is contradictory to Liu and Reitz's experimental findings [43]. Thus, Liu and Reitz [43] proposed a sheet-thinning breakup mechanism (for $80 < We < 350$) which is consistent with their experimental results. In this sheet-thinning breakup mechanism, the droplet first deforms into a disc-like shape with the thickness growing thinner from the center to the edge; then the periphery of the flattened drop is bent in the direction of the flow due to its low inertia, forming a liquid sheet which disintegrates into ligaments and droplets. Since numerical methods can provide more flow details which can help understand the atomisation mechanism, many simulations of droplet breakup have been carried out [27,46–50]. However, most of these published numerical studies to date have been limited to liquid/gas density ratios only of order 1–100. Since the majority of atomisation experiments are carried out in air at atmospheric pressure with high density liquids, experimental data are mainly available for density ratios a factor of 10 greater, and thus quantitative comparison between numerical modelling and experiment is quite rare. In the present simulations of droplet breakup, water is used as the liquid and air at atmospheric pressure is used as the gas, resulting in a high density ratio of 830. The drop breakup mechanism will then be analysed and the breakup mechanism proposed based on the simulation results.

The effect of liquid viscosity is to retard the drop deformation process and thus hinder breakup, and when viscous effects are significant, this can affect the critical Weber number We_{cr} that separates breakup and deformation modes. In order to characterise this effect, the Ohnesorge number ($Oh = \mu_L/\sqrt{\rho_L D_0 \sigma}$) may be introduced as the ratio of the liquid viscous force to the surface tension force. Empirical correlations between We_{cr} and Oh have been proposed by Pilch and Erdman [51] ($We_{cr} = We_{cr0}(1 + 1.077Oh^{1.6})$) and Gelfand [52] ($We_{cr} = We_{cr0}(1 + 1.5Oh^{0.74})$) based on experimental data. Cohen [53] has also proposed a semi-empirical correlation based on analysis of energy transfer in secondary breakup ($We_{cr} = We_{cr0}(1 + C\,Oh)$ where C has a value between 1.0 and 1.8). The proposed empirical correlations differ significantly from each other due to inaccuracies in the experimental measurements. An initiation time - defined as the time required for a drop to deform beyond oblate ellipsoid shape - has been identified for a range of Oh values [37,51], with several correlation functions proposed by Pilch and Erdman [51], Hsiang and Faeth [54] and

Gelfand et al. [55]. However, significant discrepancies may be observed between these correlations. Therefore, the opportunity is taken here to use the developed numerical technique to investigate the influence of liquid viscosity on drop deformation and breakup.

The present two-phase flow solver is developed using an existing multi-block structured mesh code for LES of single phase constant density turbulent flow [56–58]. In the following sections, the two-phase flow governing equations and numerical methods are first described. Validation test cases covering interface instability and drop formation in laminar liquid jets are presented next. Finally, the mechanism of droplet breakup and influence of liquid viscosity are examined using the developed numerical technique.

2. Formulation of two-phase flow governing equations

The philosophy for the current approach to two-phase flow simulation is to adopt the usual spatially filtered LES formulation [59], with an overbar used to represent spatial filtering. Thus for any variable Ψ, its spatially filtered value is given by:

$$\overline{\Psi}(x,t)=\int_{-\infty}^{\infty}G(x-\xi)\Psi(\xi,t)\,\mathrm{d}\xi \quad where \quad \int_{-\infty}^{\infty}G(\xi)\,\mathrm{d}\xi=1 \tag{1}$$

where G is the filter kernel. In the present formulation a box filter is used [59].

Since both liquid and gas are assumed to be incompressible and immiscible, the continuity equation is then everywhere the same as in single phase flows, and its filtered version reads:

$$\frac{\partial\overline{U}_i}{\partial x_i}=0 \tag{2}$$

where U_i is the instantaneous velocity. After filtering, the nonlinearity of the convection terms leads to the appearance of a residual or sub-grid-scale (SGS) stress tensor (τ_{ij}^{SGS} as defined below) in the filtered momentum equations:

$$\frac{\partial(\overline{U}_i)}{\partial t}+\frac{\partial(\overline{U}_i\overline{U}_j)}{\partial x_j}=-\frac{1}{\rho}\frac{\partial\overline{P}}{\partial x_i}+\frac{1}{\rho}\frac{\partial(\overline{\tau}_{ij}^{mol}+\tau_{ij}^{SGS})}{\partial x_j}+g_i+\frac{1}{\rho}\tilde{F}_i^{ST} \tag{3}$$

$$\tau_{ij}^{SGS}=\rho(\overline{U_iU_j}-\overline{U}_i\overline{U}_j) \tag{4}$$

where P is pressure, g_i is gravitational acceleration, τ_{ij}^{mol} represents the molecular viscous stress. $\tilde{F}_i^{ST}$ is the singular surface tension force located on the filtered interface which is constructed by the surface-averaging filter kernel proposed by Pitsch [60] for a flame front. A simple Smagorinsky eddy viscosity approach is used here, where $\triangle$ is used to represent the filter width (taken here as the cube root of the local computational cell volume, with the value of the Smagorinsky constant C_S set in all calculations to be 0.1); the full expressions for the diffusion terms become:

$$\overline{\tau}_{ij}^{mol}=2\mu\overline{S}_{ij}\quad \tau_{ij}^{SGS}=2\mu^{SGS}\overline{S}_{ij}\quad \overline{S}_{ij}=\frac{1}{2}\left(\frac{\partial\overline{U}_i}{\partial x_j}+\frac{\partial\overline{U}_j}{\partial x_i}\right)$$
$$\mu^{SGS}=\rho(C_S\triangle)^2\overline{S}\quad \overline{S}=\sqrt{2\overline{S}_{ij}\overline{S}_{ij}} \tag{5}$$

$\overline{S}_{ij}$ is the resolved strain rate tensor, with magnitude $\overline{S}$. Since the interface is tracked explicitly in the current formulation, density and viscosity are treated sharply to maintain the physical discontinuity across the interface, and thus are set to be the properties of liquid/gas depending on the local value of the resolved LS variable $\tilde{\phi}$ ($\tilde{\phi}$ is the LS representation of the filtered interface as detailed below):

$$\rho=\rho_G+(\rho_L-\rho_G)H(\tilde{\phi})\quad \mu=\mu_G+(\mu_L-\mu_G)H(\tilde{\phi})$$
$$H(\tilde{\phi})=\begin{cases}1 & \text{if } \tilde{\phi}>0\\ 0 & \text{if } \tilde{\phi}\le 0\end{cases} \tag{6}$$

$H(\tilde{\phi})$ is the Heaviside function; subscripts G and L indicate gas and liquid properties respectively.

For the filtered momentum equations, it remains only to express the filtered surface tension in terms of resolved variables. As noted above, SGS surface tension modelling is so far rather immature and still under development; furthermore, it has not been well validated against experimental data particularly for the high liquid/gas density ratios of interest here. For these reasons, no SGS component of the surface tension force has been included, and the resolved surface tension force is computed directly from the morphology of the filtered interface:

$$\tilde{F}_i^{ST}=\sigma\tilde{\kappa}\frac{\partial H}{\partial x_i}\quad \tilde{\kappa}=\frac{\partial\tilde{n}_i}{\partial x_i}\quad \tilde{n}_i=-\frac{1}{\sqrt{\frac{\partial\tilde{\phi}}{\partial x_k}\frac{\partial\tilde{\phi}}{\partial x_k}}}\frac{\partial\tilde{\phi}}{\partial x_i} \tag{7}$$

Here, σ is the surface tension coefficient. $\tilde{\kappa}$ and $\tilde{n}_i$ are respectively the curvature and normal vector (pointing from the liquid phase into the gas) of the filtered interface.

Since both liquid and gas phases are viscous, the jump condition on the interface is (readers are referred to [61,62] for more details):

$$[\overline{U}_i]=0 \tag{8}$$

$$\left[\overline{P}-\tilde{n}_i\left(\overline{\tau}_{ij}^{mol}+\tau_{ij}^{SGS}\right)\tilde{n}_j\right]=\sigma\overline{\kappa} \tag{9}$$

Finally, the LES version of the scalar advection equations which determine the interface movement is derived. Oberlack et al. [63] showed that the classical Reynolds ensemble averaging and some LES SGS models violated the generalized scaling symmetry of the G-equation (which reduces to LS equation when the laminar burning velocity is set to be 0). A consistent formulation of the G-equation for the filtered flame front based on a new filtering technique was proposed by Pitsch [60,64]. Following Pitsch's procedure [60,64], the LS equation which governs the evolution of the filtered interface is given as follows:

$$\frac{\partial\tilde{\phi}}{\partial t}+\overline{U}_i\frac{\partial\tilde{\phi}}{\partial x_i}=0 \tag{10}$$

where $\tilde{\phi}$ is the LS representation of the filtered interface rather than the filtered LS field, and is the signed distance to the filtered interface.

In order to reproduce a sharp interface by the VOF method in the LES formulation, the spatial filtering operation defined by Eq. (1) can not be applied to the VOF field and VOF advection equation. To be consistent with the LS representation and keep a sharp interface, the resolved VOF field $\tilde{F}$ in the LES is the liquid volume fraction determined by the filtered interface rather than the spatially filtered VOF field. $\tilde{F}$ is evolved by the filtered velocity field, and the contribution of the SGS term is neglected, resulting in a scalar advection equation with the same form as the LS equation:

$$\frac{\partial\tilde{F}}{\partial t}+\overline{U}_i\frac{\partial\tilde{F}}{\partial x_i}=0 \tag{11}$$

Some further justification for neglect of SGS surface tension and SGS interface dynamics here was provided by the observation that the liquid flow is laminar in the jet/drop breakup simulations reported below and thus no SGS interface deformation is induced by any SGS velocity in the liquid field. Marmottant and Villermaux demonstrate in their experiments (Fig. 42 in [65]) that a smooth interface and axisymmetric deformation are observed for an injected laminar liquid jet while irregular interface distortions are observed right after a turbulent liquid jet exits the nozzle. This is also confirmed in the LES of a liquid jet in coaxial air flow by Xiao et al. [66]. In the liquid jet/drop deformation period, both experiments (Fig. 1 in [67], Fig. 7 in [41]) and the current simulations

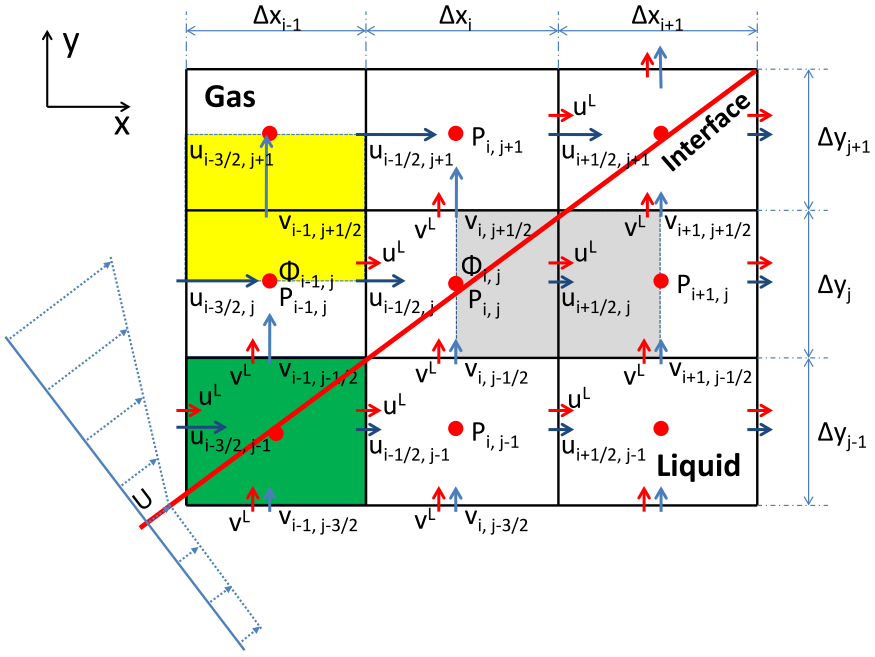

Fig. 1. Grid and variable arrange ment. Green shaded region is pressure control volume (CV); grey-shaded region is x-momentum CV; yellow-shaded region is y-momentum CV. The red line represents the interface. (For interpretation of the references to colour in this figure legend, the reader is referred to the web version of this article.)

give smooth axisymmetric deformation without any irregular interface distortions, implying that the velocity field in the liquid phase for the simulations presented here is laminar.

Although the gas flow is turbulent, the SGS gaseous eddies do not have enough energy to directly distort the interface as the liquid has a high inertia arising from its high density in comparison with the gas. LES of a liquid jet in air crossflow by Xiao et al. [68] shows that the large eddies in the incoming air flow do not cause any deformation of the liquid column due to the high liquid/gas density ratio. Therefore, the less energetic SGS eddies in the gas phase are unable to contribute to the interface deformation.

Since solution of the Level Set Eq. (10) does not guarantee satisfaction of the signed distance property ($\left|\nabla\tilde{\phi}\right| = 1$), a re-initialisation equation is solved:

$$\frac{\partial\varphi}{\partial\tau} = S(\varphi_0)\left(1 - \sqrt{\frac{\partial\varphi}{\partial x_k}\frac{\partial\varphi}{\partial x_k}}\right) \quad S(\varphi_0) = \frac{\varphi_0}{\sqrt{\varphi_0{}^2 + d^2}} \tag{12}$$

Re-initialisation is carried out for a pseudo-level set variable φ in pseudo-time τ. φ is initialised ($\tau = 0$) to equal the solution of the physical (resolved) level set Eq. (10) at time t, i.e., $\varphi_0 = \varphi(\tau = 0) = \tilde{\phi}(t)$. The steady state ($\tau \to \infty$) solution for φ is a signed distance to the resolved interface $\tilde{\phi}(t) = 0$, and is used to correct $\tilde{\phi}$ at time t to ensure it obeys the signed distance property, i.e., $\tilde{\phi}(t) = \varphi(\tau \to \infty)$.

In what follows, for simplicity the overbar indicating spatial filtering has been omitted, but all variables represent LES resolved quantities.

3. Numerical details

The present two-phase flow solver was developed using a Cartesian staggered mesh. For convenience the methodology and discretisation scheme is illustrated here in 2D for simplicity though it is actually implemented in 3D in the code, with details provided in [26]. The grid and variable arrangement are shown in Fig. 1; pressure, ϕ, F, ρ, and μ are located at cell centres; the velocity components are located at corresponding faces. u and v are the velocity components obtained after solution of the governing equations outlined in the previous section, while u^L and v^L are the components of a liquid velocity field constructed by an extrapolation and divergence-free approach as detailed below.

The implementation of the present CLSVOF method is described in [26,66,68,69]. A detailed description of the overall algorithm, including the way in which F and ϕ solutions are combined to deliver the transient dynamics of the interface geometry (interface reconstruction, and F/ϕ field evolution), has been outlined in full in [26]. In brief, 2nd order accurate operator split methods [24] are used in both F and ϕ equations. The interface normal vector is calculated from the level set gradient ($d\phi$) by a proper choice of forward difference (d^+), central difference (d^c), and backward difference (d^-): when the level set is determined by one interface ($|d^+ - d^-| < 0.01$), $d\phi = d^c$; when two interfaces are close ($|d^+ - d^-| \geq 0.01$), if $|d^+| \geq |d^-|$, $d\phi = d^+$, otherwise $d\phi = d^-$;. Then the interface is translated along the normal direction in order to ensure compatibility with both F and ϕ solutions within each cell. Numerical tests (see [26]) have shown that, when combined with the CLSVOF approach, this allows good accuracy of interface tracking simultaneously with ensuring low liquid mass errors. The extrapolated liquid velocity is used also in the LS and VOF advection equations following [24]. Emphasis is placed on providing full details of the creation of the extrapolated velocity field, and its use in the discretisation of the governing equations in the following description.

3.1. Temporal discretisation

The LES code for single phase flow used as the starting point for the present work [56] had adopted the classical techniques of a centred 2nd order method for all spatial discretisation and a 2nd order Adams–Bashforth scheme for temporal advancement. In single phase flows, convection and diffusion terms are continuous in both time and space. However, in the present application these terms are discontinuous across the liquid/gas interface. Convection and diffusion terms will be discontinuous in time in any cell where the phase changes from gas to liquid (or vice-versa) during a time

step. Since the Adams-Bashforth scheme is based on Taylor series expansion and requires continuity of convection and diffusion terms, this may cause local errors for two-phase flow. For caution's sake therefore, a simple 1st order forward Euler projection method was used for temporal discretisation of the two-phase flow equations. Since explicit time-marching was involved, and the associated CFL_{max} constraint in LES calculations means the time step is usually very small (typically for the simulations presented below CFL_{max} was $O(0.1)$), any associated error should be negligible, as was confirmed by a time-step sensitivity study for single droplet breakup [69].

An intermediate velocity field (U_i^*) is first computed from a version of the solution of momentum equations which includes convection, molecular and SGS diffusion, and gravitational terms (Note that surface tension is treated as part of the pressure term using the approach to be described in sub-Section 3.4):

$$\frac{U_i^* - U_i^n}{\delta t} = -\frac{\partial (U_i^n U_j^n)}{\partial x_j} + \frac{1}{\rho^n}\frac{\partial (\tau_{ij}^{mol^n} + \tau_{ij}^{SGS^n})}{\partial x_j} + g_i \tag{13}$$

The intermediate velocity field U_i^* is updated using a pressure gradient to obtain the velocity field $n+1$:

$$\frac{U_i^{n+1} - U_i^*}{\delta t} = -\frac{1}{\rho^n}\frac{\partial P^{n+1}}{\partial x_i} \tag{14}$$

Since the velocity field at time step $n+1$ must satisfy the continuity equation, a pressure Poisson equation may be derived by taking the divergence of the above equation, whose solution allows P^{n+1} to be calculated:

$$\frac{\partial}{\partial x_i}\left(\frac{1}{\rho^n}\frac{\partial P^{n+1}}{\partial x_i}\right) = \frac{1}{\delta t}\frac{\partial U_i^*}{\partial x_i} \tag{15}$$

P^{n+1} is then used in Eq. (14) to update the intermediate velocity field to establish U_i^{n+1}.

3.2. Extrapolated liquid velocity and divergence-free approach

The philosophy of using an extrapolated liquid velocity field is based on the strong discontinuity of the velocity gradient across the interface observed in two-phase flow with high density and viscosity ratio. For the two-phase shear flow in equilibrium demonstrated in Fig. 1, the high liquid/gas viscosity ratio ($O(100)$) indicates that the velocity gradient in the gas is much larger than that in the liquid as the shear stress is the same across the interface. Therefore, the spatial discretisation of the governing equations in the vicinity of the interface must be carefully designed to tackle this discontinuity.

In the following, the discretisation of the momentum equation for u in x-momentum CVs is examined. When the level set value at a CV node is positive, this CV is referred to as a liquid CV, otherwise, it is referred to as a gas CV. For example, since $\phi_{i+1/2,\,j} > 0$, the x-momentum CV $\Omega_{i+1/2,\,j}$ is a liquid CV, and it is treated as if it contains only liquid: the resolved velocity $u_{i+1/2,\,j}$ thus represents a liquid velocity, and the density in this x-momentum CV is set to be liquid density (i.e. $\rho_{i+1/2,\,j} = \rho_L$). Similarly, due to $\phi_{i-1/2,\,j} > 0$, the x-momentum CV $\Omega_{i-1/2,\,j}$ is considered as a gas CV: the resolved velocity $u_{i-1/2,\,j}$ represents the gas velocity, and the density in this x-momentum CV is set to be gas density (i.e. $\rho_{i-1/2,\,j} = \rho_G$). When solving for the gas velocity $u_{i-1/2,\,j}$ from the momentum equation in the gas CV $\Omega_{i-1/2,\,j}$, the gas momentum flux at the right face $\rho_G u_{i,\,j} u_{i,\,j}$ needs to be computed. When solving for the liquid velocity $u_{i+1/2,\,j}$ from the momentum equation in the liquid CV $\Omega_{i+1/2,\,j}$, the liquid momentum flux at the left face $\rho_L u_{i,\,j} u_{i,\,j}$ needs to be computed. In this sense, the borderline between these two CVs is numerically treated as the two-phase interface, and $u_{i,\,j}$ should therefore represent the interface velocity in the numerical approach. As a consequence of the fact that the interface velocity is much closer to that in neighbouring liquid CVs than in neighbouring gas CVs, a good approximation to $u_{i,\,j}$ is to extrapolate the velocity in the neighbouring liquid CV to this point. For convenience, the extrapolated liquid velocity at the gas CV node $u^L_{i-1/2,\,j}$ (indicated by the red arrow labelled u^L in Fig. 1) is first calculated, and then $u_{i,\,j}$ is computed from arithmetic averaging $u_{i,\,j} = (u^L_{i-1/2,\,j} + u_{i+1/2,\,j})/2$. This issue can also be explained in another way. Since the liquid/gas density ratio is large ($O(1000)$), any error in $u_{i,\,j}$ can result in a much larger error in the momentum flux term ρuu in the liquid phase than in the gas phase. Therefore, it is more important to find a proper value of $u_{i,\,j}$ so that the calculated convection term $(u_{i+1,\,j}u_{i+1,\,j} - u_{i,\,j}u_{i,\,j})/\Delta x$ in the liquid CV approximates well the physical (real) convection term $(\partial uu/\partial x)_{i+1/2,\,j}$ in the liquid phase. This demands that the computed velocity gradient $(u_{i+1,\,j} - u_{i,\,j})/\Delta x$ in the liquid CV approximate well the physical value $(\partial u/\partial x)_{i+1/2,\,j}$ in the liquid phase. The simple averaging treatment (i.e. $u_{i,\,j} = (u_{i-1/2,\,j} + u_{i+1/2,\,j})/2$) in the conventional discretisation approach would considerably overpredict the velocity gradient in the liquid CV because of the use of the gas velocity $u_{i-1/2,\,j}$, resulting in significant numerical error in momentum. Use of an extrapolated liquid velocity approach is a better option in this case as demonstrated below.

To implement the extrapolated liquid velocity technique, a separate array U_i^L was created (with components u^L and v^L in 2D) as follows:

i. U_i^L at liquid phase nodes ($\phi > 0$) was set equal to the momentum-equation-deduced velocity U_i:

$$u^L_{i-1/2,j} = u_{i-1/2,j} \text{ if } \phi_{i-1/2,j} > 0 \quad \text{where } \phi_{i-1/2,j} = \frac{\phi_{i-1,j} + \phi_{i,j}}{2}$$
$$v^L_{i,j-1/2} = v_{i,j-1/2} \text{ if } \phi_{i,j-1/2} > 0 \quad \text{where } \phi_{i,j-1/2} = \frac{\phi_{i,j-1} + \phi_{i,j}}{2} \tag{16}$$

ii. U_i^L at gas phase nodes ($\phi < 0$) was computed by outwards extrapolation along the interface normal from liquid into gas. For example, the liquid velocity component u^L at gas phase nodes close to the interface was calculated by solving the following extrapolation equation to steady state:

$$\frac{\partial u^L}{\partial \tau} + n_i \frac{\partial u^L}{\partial x_i} = 0 \quad \text{if } \phi \le 0 \tag{17}$$

A forward Euler scheme was used for discretisation of this extrapolation equation in pseudo-time τ:

$$\frac{u^{L\,n+1}_{i-1/2,j} - u^{L\,n}_{i-1/2,j}}{\Delta \tau} = -\left(n_x \frac{\partial u^L}{\partial x}\right)^n_{i-1/2,j} - \left(n_y \frac{\partial u^L}{\partial y}\right)^n_{i-1/2,j} \tag{18}$$

where the pseudo time step $\Delta\tau$ was set to be $0.3\min(\Delta x_{i-1}, \Delta x_i, \Delta y_{j-1}, \Delta y_j, \Delta y_{j+1})$. This equation is solved for 8 time steps to create an extrapolated liquid velocity in a two-cell thick layer on the gas phase side of the interface. And a first order upwind scheme was used for spatial discretisation, e.g.:

$$\left(\frac{\partial u^L}{\partial x}\right)_{i-1/2,j} = \begin{cases} \dfrac{u^L_{i-1/2,j} - u^L_{i-3/2,j}}{\Delta x_{i-1}} & \text{if } (n_x)_{i-1/2,j} > 0 \\ \dfrac{u^L_{i+1/2,j} - u^L_{i-1/2,j}}{\Delta x_i} & \text{if } (n_x)_{i-1/2,j} \le 0 \end{cases} \tag{19}$$

Since the extrapolated liquid velocity field will not automatically be divergence-free, the liquid velocity field calculated at the gas nodes must be corrected to satisfy the continuity equation. First, a liquid velocity source term in a typical cell (i, j) was computed:

$$S = u^L_{i-1/2,j}\Delta y_j - u^L_{i+1/2,j}\Delta y_j + v^L_{i,j-1/2}\Delta x_i - v^L_{i,j+1/2}\Delta x_i \tag{20}$$

The extrapolated liquid velocity was then corrected by an upwind scheme:

$$u^L_{i-1/2,j} = u^L_{i-1/2,j} - a_w \frac{S}{A}|n_x|_{i-1/2,j}$$
$$u^L_{i+1/2,j} = u^L_{i+1/2,j} + a_e \frac{S}{A}|n_x|_{i+1/2,j} \tag{21}$$

$$v^L_{i,j-1/2} = v^L_{i,j-1/2} - a_s \frac{S}{A}|n_y|_{i,j-1/2} \quad v^L_{i,j+1/2} = v^L_{i,j+1/2} + a_n \frac{S}{A}|n_y|_{i,j+1/2} \tag{22}$$

where A is the projected cell face area and the coefficients are given by:

$$a_w = \begin{cases} 1 & \text{if } (\phi_{i-1/2,j} < 0 \text{ and } \phi_{i,j} > \phi_{i-1,j}) \\ 0 & \text{else} \end{cases} \tag{23}$$

$$a_e = \begin{cases} 1 & \text{if } (\phi_{i+1/2,j} < 0 \text{ and } \phi_{i,j} > \phi_{i+1,j}) \\ 0 & \text{else} \end{cases} \tag{24}$$

$$a_s = \begin{cases} 1 & \text{if } (\phi_{i,j-1/2} < 0 \text{ and } \phi_{i,j} > \phi_{i,j-1}) \\ 0 & \text{else} \end{cases} \tag{25}$$

$$a_n = \begin{cases} 1 & \text{if } (\phi_{i,j+1/2} < 0 \text{ and } \phi_{i,j} > \phi_{i,j+1}) \\ 0 & \text{else} \end{cases} \tag{26}$$

$$A = a_w|n_x|_{i-1/2,j}\Delta y_j + a_e|n_x|_{i+1/2,j}\Delta y_j + a_s|n_y|_{i,j-1/2}\Delta x_i + a_n|n_y|_{i,j+1/2}\Delta x_i \tag{27}$$

Eqs. (20) , (21), and (22) were solved for sufficient time steps (typically 4) to create a continuity-satisfying extrapolated liquid velocity in a two-cell thick layer on the gas phase side of the interface.

3.3. Spatial discretisation for momentum equation

In general, a centered 2nd order approximation is followed using a classical finite-volume approach, leading to the need to evaluate cell face convective and diffusive fluxes. For the momentum equations the approach adopted deviates from the classical form in terms of how the liquid extrapolated velocity is used in the convective flux (this then also applies to the F and ϕ equations), and how the cell face density and effective viscosity are chosen in the diffusive flux. The practices adopted are illustrated here by considering a single convective and diffusive contribution as examples. Each momentum CV is treated as either liquid or gas depending on the sign of the Level Set at the node for that CV. For example, if the ϕ value at the $u_{i-1/2,j}$ node of the x-momentum CV $\Omega_{i-1/2,j}$ (Fig. 1) is greater than zero, it is a treated as a liquid CV, the resolved velocity at the node represents a liquid velocity and the density for this CV is set to the liquid density; otherwise gas density is used, thus:

$$\rho_{i-1/2,j} = \begin{cases} \rho_L & \text{if } \phi_{i-1/2,j} > 0 \\ \rho_G & \text{if } \phi_{i-1/2,j} \le 0 \end{cases} \qquad \phi_{i-1/2,j} = \frac{\phi_{i-1,j} + \phi_{i,j}}{2} \tag{28}$$

Considering for illustration purposes a typical x-momentum convective term in a cell intersected by the interface, to reduce momentum errors, the extrapolated velocity is introduced into the discretisation following the rules indicated below:

$$\int_{\Omega_{i-1/2,j}} \frac{\partial uu}{\partial x}\,dV = \begin{cases} (u^L_{i,j}u^L_{i,j} - u^L_{i-1,j}u^L_{i-1,j})\Delta y_j & \text{if } \phi_{i-1/2,j} > 0 \\ (C_{i,j} - C_{i-1,j})\Delta y_j & \text{if } \phi_{i-1/2,j} \le 0 \end{cases} \tag{29}$$

where

$$C_{i,j} = \begin{cases} u^L_{i,j}u^L_{i,j} & \text{if } \phi_{i+1/2,j} > 0 \\ u_{i,j}u_{i,j} & \text{if } \phi_{i+1/2,j} \le 0 \end{cases}$$
$$C_{i-1,j} = \begin{cases} u^L_{i-1,j}u^L_{i-1,j} & \text{if } \phi_{i-3/2,j} > 0 \\ u_{i-1,j}u_{i-1,j} & \text{if } \phi_{i-3/2,j} \le 0 \end{cases} \tag{30}$$

$$u^L_{i,j} = \frac{u^L_{i-1/2,j} + u^L_{i+1/2,j}}{2} \quad u_{i,j} = \frac{u_{i-1/2,j} + u_{i+1/2,j}}{2} \tag{31}$$

Similarly, considering a typical diffusion term in the x-momentum equation, special care must be taken to respect the discontinuous nature of density and effective viscosity across the gas/liquid interface:

$$\int_{\Omega_{i-1/2,j}} \frac{1}{\rho}\frac{\partial\left(\tau^{mol}_{xx} + \tau^{SGS}_{xx}\right)}{\partial x}\,dV = \int_{\Omega_{i-1/2,j}} \frac{1}{\rho}\frac{\partial \tau^{eff}_{xx}}{\partial x}\,dV \tag{32}$$

$$= \frac{1}{\rho_{i-1/2,j}}\left(\tau^{eff}_{xx\,i,j} - \tau^{eff}_{xx\,i-1,j}\right)\Delta y_j \tag{33}$$

where, for example:

$$\tau^{eff}_{xx\,i,j} = 2\mu^{eff}_E\left(\frac{\partial u}{\partial x}\right)_{i,j} = 2\mu^{eff}_E\left(\frac{u_{i+1/2,j} - u_{i-1/2,j}}{\Delta x_i}\right)$$
$$\mu^{eff}_E = \mu_E + \mu^{SGS}_E \tag{34}$$

μ^{eff}_E is the effective viscosity at the east face of the x-momentum control volume $\Omega_{i-1/2,j}$. This face is co-incident with the pressure node (i, j). Thus, for most cells the value of μ^{eff} calculated at (i, j) can be used for μ^{eff}_E; however, care must be taken for momentum nodes which lie close to the interface. The practice followed is: an effective viscosity $\mu^{eff}_{i,j}$ is calculated and stored at the nodes of pressure CVs:

$$\mu^{eff}_{i,j} = \begin{cases} \mu_G + \rho_G(C_s\Delta)^2 S_{i,j} & \text{if } \phi_{i,j} \le 0 \\ \mu_L + \rho_L(C_s\Delta)^2 S^L_{i,j} & \text{if } \phi_{i,j} > 0 \end{cases} \tag{35}$$

Where $S_{i,j}$ and $S^L_{i,j}$ are the magnitude of the resolved strain rate tensor at node (i, j) evaluated using momentum-equation-deduced velocity field and liquid velocity field respectively. Next, the eddy viscosity at face E of the momentum cell is determined. In Eq. (34), velocities $u_{i-1/2,j}$ and $u_{i+1/2,j}$ are used to calculate the effective stress $\tau^{eff}_{xx\,i,j}$. When both x-momentum CVs $\Omega_{i-1/2,j}$ and $\Omega_{i+1/2,j}$ are liquid ($\phi_{i-1/2,j} > 0$ and $\phi_{i+1/2,j} > 0$), $(u_{i+1/2,j} - u_{i-1/2,j})/\Delta x_i$ represents a velocity gradient in the liquid phase, and thus an effective eddy viscosity defined using liquid fluid properties and liquid velocities is used for μ^{eff}_E:

$$\mu^{eff}_E = \begin{cases} \mu^{eff}_{i,j} & \text{if } \phi_{i,j} > 0 \\ \dfrac{a_{i-1,j}\mu^{eff}_{i-1,j} + a_{i+1,j}\mu^{eff}_{i+1,j}}{a_{i-1,j} + a_{i+1,j}} & \text{if } \phi_{i,j} \le 0 \end{cases}$$
$$a_{i,j} = \begin{cases} 1 & \text{if } \phi_{i,j} > 0 \\ 0 & \text{if } \phi_{i,j} \le 0 \end{cases} \tag{36}$$

When $\phi_{i-1/2,j} \le 0$ or $\phi_{i+1/2,j} \le 0$, $u_{i-1/2,j}$ or $u_{i+1/2,j}$ are gaseous velocities, $(u_{i+1/2,j} - u_{i-1/2,j})/\Delta x_i$ is an approximation to the velocity gradient in the gas phase, and thus the effective eddy viscosity defined by gas fluid properties and gas velocities should be used for μ^{eff}_E:

$$\mu^{eff}_E = \begin{cases} \mu^{eff}_{i,j} & \text{if } \phi_{i,j} \le 0 \\ \dfrac{b_{i-1,j}\mu^{eff}_{i-1,j} + b_{i+1,j}\mu^{eff}_{i+1,j}}{b_{i-1,j} + b_{i+1,j}} & \text{if } \phi_{i,j} > 0 \end{cases}$$

$$b_{i,j} = \begin{cases} 1 & \text{if } \phi_{i,j} \le 0 \\ 0 & \text{if } \phi_{i,j} > 0 \end{cases} \tag{37}$$

Readers are referred to [26] for calculation of other diffusion terms.

3.4. Surface tension term - Ghost Fluid method

In the current simulations, the interfacial pressure jump arising from surface tension is incorporated into the discretisation of the pressure gradient following the Ghost Fluid Method [70–72]. If the two-phase interface is located between nodes $(i-1, j)$ and (i, j), the pressure gradient at face $(i-1/2, j)$ is discretised as:

$$\left(\frac{\partial P}{\partial x}\right)_{i-1/2,j} = \frac{P_{i,j} - [P]_\sigma - P_{i-1,j}}{\Delta x} \tag{38}$$

Here, $[P]_\sigma$ is the pressure jump across the interface due to the surface tension:

$$[P]_\sigma = \begin{cases} \sigma\kappa_\Gamma & \text{if } \phi_{i-1,j} \le 0 \text{ and } \phi_{i,j} > 0 \\ -\sigma\kappa_\Gamma & \text{if } \phi_{i-1,j} > 0 \text{ and } \phi_{i,j} \le 0 \\ 0 & \text{otherwise} \end{cases} \tag{39}$$

The curvature at the interface κ_Γ is calculated using linear interpolation:

$$\kappa_\Gamma = \kappa_{i-1,j}(1-\theta) + \kappa_{i,j}\theta \quad \theta = \frac{|\phi_{i-1,j}|}{|\phi_{i-1,j}| + |\phi_{i,j}|} \tag{40}$$

where $\kappa_{i,j}$ is calculated from derivatives of the Level Set function [16].

3.5. Pressure Poisson equation

The Poisson Eq. (15) is discretised by integration over $\Omega_{i,j}$ (see Fig. 1), and has the form in 2D:

$$\int_{\Omega_{i,j}} \left[\frac{\partial}{\partial x}\left(\frac{1}{\rho}\frac{\partial P}{\partial x}\right) + \frac{\partial}{\partial y}\left(\frac{1}{\rho}\frac{\partial P}{\partial y}\right)\right] dV = \frac{1}{\Delta t}\int_{\Omega_{i,j}} \left(\frac{\partial u^*}{\partial x} + \frac{\partial v^*}{\partial y}\right) dV \tag{41}$$

The pressure Laplace operator is discretised via:

$$\int_{\Omega_{i,j}} \left[\frac{\partial}{\partial x}\left(\frac{1}{\rho}\frac{\partial P}{\partial x}\right)\right] dV = \left[\frac{1}{\rho_{i+1/2,j}}\left(\frac{\partial P}{\partial x}\right)_{i+1/2,j} - \frac{1}{\rho_{i-1/2,j}}\left(\frac{\partial P}{\partial x}\right)_{i-1/2,j}\right]\Delta y_j \tag{42}$$

Pressure gradients are discretised as described in sub-Section 3.4, incorporating surface tension effects via the ghost fluid method. The density is treated sharply as in Eq. (28). The source term is discretised as:

$$\int_{\Omega_{i,j}} \left(\frac{\partial u^*}{\partial x} + \frac{\partial v^*}{\partial y}\right) dV = (u^*_{i+1/2,j} - u^*_{i-1/2,j})\Delta y_j + (v^*_{i,j+1/2} - v^*_{i,j-1/2})\Delta x_j \tag{43}$$

When solving the pressure Poisson equation in two-phase flows, one can assume $[\frac{1}{\rho}\nabla P] = 0$, where $[\,]$ denotes the jump across the interface [71,72]. Thus, $\frac{1}{\rho}\nabla P$ is continuous across the interface although there is a jump in ∇P due to the density discontinuity. The standard multigrid method for solving elliptic PDEs, in particular the bilinear interpolation operator, implicitly relies on continuity of ∇P. A more appropriate interpolation operator is one that can exploit the continuity of $\frac{1}{\rho}\nabla P$. Operator-induced interpolation is the optimum route to achieve this and was implemented in the Box multigrid method (BoxMG) by Dendy[73,74]. The BoxMG code is available (see [75]), and its implementation into the code used here is given in [26]. For two-phase flows containing complex interfaces and strong discontinuity, combining the multigrid method with a preconditioned conjugate method improves both robustness and scalability [76], and this is the solution route adopted here.

4. Results

4.1. Preliminary tests of extrapolated liquid velocity approach

Four preliminary tests are carried out in this subsection to demonstrate the superiority of the extrapolated liquid velocity approach, with water used as the liquid and atmospheric air as the gas. The air density ρ_G and dynamic viscosity μ_G were $1.272 kg/m^3$ and $1.86 \times 10^{-5} Pa \cdot s$; the water density ρ_L and dynamic viscosity μ_L were $1002 kg/m^3$ and $0.892 \times 10^{-3} Pa \cdot s$ respectively. The simulation domain size is $[0\ 28.8] \times [-9\ 9] \times [-9\ 9]$ mm in the x, y, and z directions respectively. A uniform fine mesh is used in the region $[0\ 28.8] \times [-4.74\ 4.74] \times [-4.74\ 4.74]$ mm with a cell size of 0.12 mm (i.e. $\sim D_0/25$, where D_0 is the initial droplet diameter.). In other regions of the simulation domain, a coarser mesh is used to reduce the computational cost.

An illustration of the improved performance when the liquid velocity extrapolation technique was used is provided in Fig. 2, for an initially static water droplet in a uniform airflow. The drop diameter was 3.1 mm with drop centre located initially at (8,0,0) mm, and the gas velocity was 15.7 m/s. To exclude the pressure jump across the interface, in and only in this test the surface tension was set to zero. The snapshot was taken 200 time steps ($\Delta t = 2 \times 10^{-7}$ second) after the simulation was initialised, when the drop is still nearly spherical. Fig. 2a shows the predicted pressure on a plane through the drop mid-section with conventional centred 2nd order accurate spatial discretisation schemes for the momentum equations [26]; the pressure field is discontinuous across the interface and contains isolated 'spikes', caused by numerical error at interface cells. It is observed in the simulations that the velocity gradient in the gas phase is much larger than that in the liquid phase due to the high density and viscosity ratio. Therefore, considerable momentum error can be introduced if the neighboring gas velocity is used for the convection term discretisation in the liquid momentum CVs. In complete contrast, a smooth pressure distribution (Fig. 2b) was correctly predicted across the interface when using the extrapolated liquid velocity approach.

The momentum error observed above with conventional discretisation can lead to numerical breakup as shown in Fig. 3(left). The surface tension coefficient σ was set to $0.072 N/m$ in this and the following two preliminary tests. This figure thus illustrates the case of an initially static water droplet exposed to a uniform air flow at a Weber number of 3.4; experiments show for this condition that no breakup but just oscillatory deformation of the drop should be observed (the detailed morphology of droplet behaviour at various *We* will be presented below in Section 4). The correct oscillatory deformation mode can be numerically reproduced only after inclusion of a liquid velocity extrapolation technique as shown in Fig. 3(right).

The importance of the extrapolated liquid velocity satisfying the continuity condition is demonstrated by simulating a moving water drop. The velocities of both the water drop and air flow are 9 m/s, resulting in a Weber number of 0, and thus the drop should therefore remain spherical. The drop diameter was 3.1 mm with drop centre located initially at (4,0,0) mm. Fig. 4 shows the morphology of the simulated drop after 1.2 ms. Without the divergence-free step for the extrapolated liquid velocity, the drop undergoes unphysical breakup due to numerical errors. With the

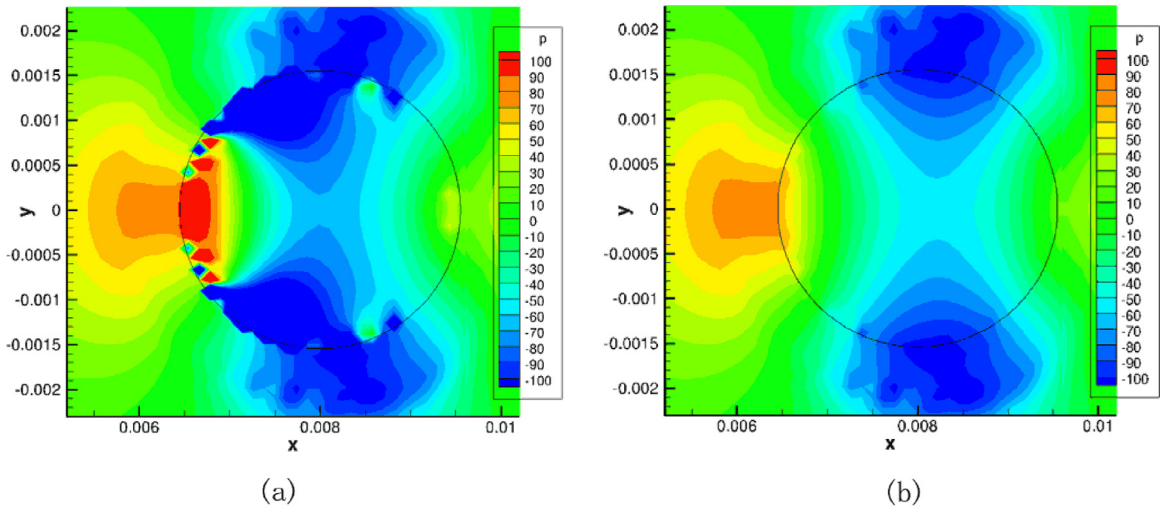

Fig. 2. (a) Conventional discretisation (b) using liquid velocity extrapolation.

Fig. 3. (Left) Numerical droplet breakup at $We = 3.4$ with conventional discretisation (Right) Predicted droplet behaviour at $We = 3.4$ with liquid velocity extrapolation.

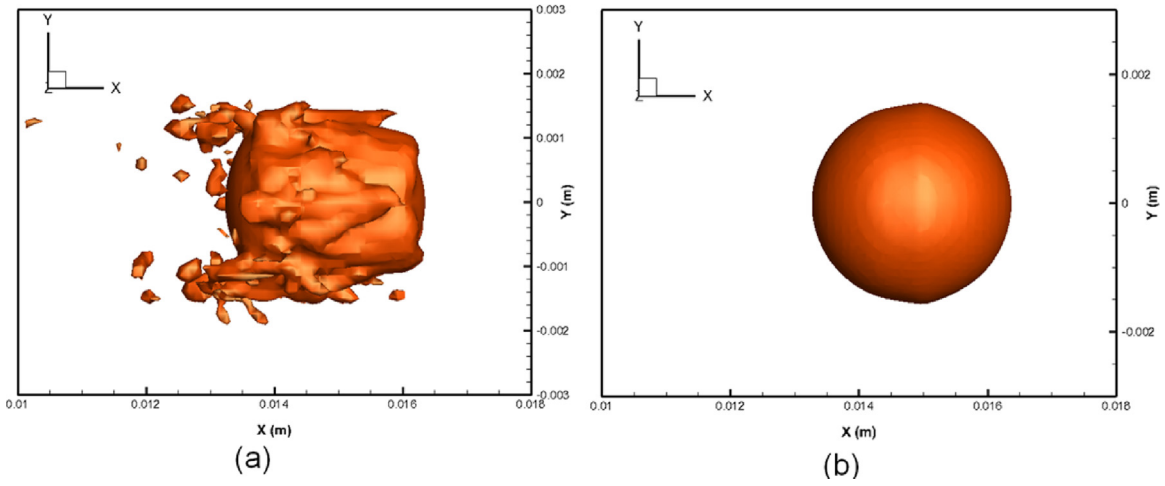

Fig. 4. Morphology of the simulated moving drop (9m/s) at $We = 0$ at 1.2 ms, (a) without or (b) with divergence-free step.

divergence-free step in the simulation, the drop almost retains its spherical shape with its center correctly moving to (14.8,0,0) mm, confirming that the implemented divergence-free algorithm can achieve satisfaction of the continuity condition for the extrapolated liquid velocity.

Finally, whilst it was momentum equation errors which motivated the introduction and design of the liquid velocity extrapolation approach adopted, it was observed that for consistency the extrapolated liquid velocity should also be used in the F and ϕ equations which determine the interface convection. Evidence to support this is given in Fig. 5 showing the predicted interface topology for the same case as in Fig. 3 of an initially static drop at the low Weber number of $We = 3.4$, where only oscillatory deformation should be seen. Fig. 5 indicates that when the momentum-equation-deduced velocity U_i is used for F and ϕ advection a considerably distorted interface is obtained, whereas with the

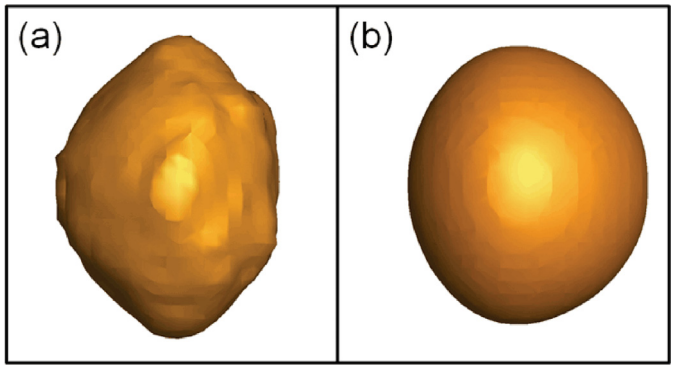

Fig. 5. Interface topology for single drop at $We = 3.4$. (a) U_i or (b) U_i^L used for F and ϕ evolution.

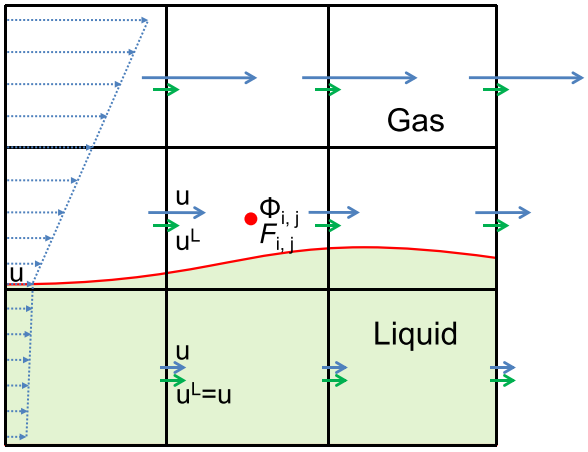

Fig. 6. Momentum equation deduced velocity (blue vector) and constructed liquid velocity (green vector) fields with red line representing the interface. (The dashed line is the assumed physical profile for the velocity component u). (For interpretation of the references to colour in this figure legend, the reader is referred to the web version of this article.)

reconstructed liquid velocity U_i^L for interface advection a smooth interface was predicted as in the experiments. The underlying reason for this difference is examined in the following. Fig. 6 shows the momentum-equation-deduced velocity and constructed liquid velocity fields (after extrapolation). Both velocity fields satisfy the continuity equation while only the momentum equation deduced velocity field is physical as it also satisfies the momentum equation. However, the physical momentum-equation-deduced velocity represents the gas velocity rather than liquid velocity in cell (i, j) in the numerical calculation. Since the shear stress is the same across the interface, the velocity gradient in the liquid is much smaller than in the gas phase because of the large liquid/gas viscosity ratio. Therefore, the velocity of the liquid phase in cell (i, j) is much closer to the velocity in the neighbouring liquid cell $(i, j-1)$. If the momentum-equation-deduced velocity is used for VOF function advection in cell (i, j), the liquid in cell (i, j) moves at the physical gas velocity, resulting in a large error. If the extrapolated liquid velocity u^L is used, much better accuracy can be obtained in the calculation of liquid volume flux.

Based on the above evidence, the liquid velocity extrapolation procedure was adopted for all two-phase flow calculations reported below.

4.2. Plateau–Rayleigh instability

Plateau–Rayleigh instability is a surface tension influenced instability occurring when a stationary liquid cylinder with initial radius R_0 is perturbed by a wave-like axially varying disturbance of initial amplitude η_0 ($\eta_0 \sin(kz)$ where z is the cylinder axial direction and k is the perturbation wavenumber, related to wavelength λ by $k = 2\pi/\lambda$). The perturbation will grow and the cylinder deform and eventually break up due to the Plateau–Rayleigh instability if $kR_0 < 1$. The perturbation grows according to $\eta(t)\sin(kz)$, with $\eta(t) = \eta_0 e^{\omega t}$ (ω is the growth rate). This problem was calculated using the fluid properties of air and water, an initial cylinder radius of $R_0 = 0.14m$ and a perturbation wavelength $\lambda = 9R_0$ ($kR_0 = 0.698$) and $\eta_0 = R_0/28 = 0.5\Delta$, where Δ is the uniform mesh spacing. The simulations were run with a domain size of $5R_0 \times 5R_0 \times 9R_0$ (uniform Cartesian mesh of $70 \times 70 \times 126$). Periodic boundary conditions were used in the z-direction, and zero-gradient conditions in the x and y directions. The predicted deformation and breakup of the liquid cylinder for this wavenumber is illustrated in Fig. 7(i), showing an initial linear phase followed by a non-linear phase leading to breakup and ligament/droplet formation. The numerically predicted growth of perturbation magnitude in the initial phase could be accurately fitted with an exponential. Four further wavenumbers were calculated and Fig. 7(ii) shows that the predicted growth rate agrees very well with the linear theory dispersion equation[77].

4.3. Laminar liquid jet breakup in stagnant air

Transition from a dripping to a jetting mode for a laminar liquid jet has been studied experimentally by Clanet and Lasheras [67]. Water was injected downward into stagnant air at a velocity V_J under gravity g, through a round tube. As the injected liquid velocity was increased, periodic dripping (PD), chaotic dripping (CD), and jetting (J) modes were observed:

- PD at very low velocity, liquid drops detach from the tube at a constant frequency, resulting in drops with constant mass. The detachment point is ~1 diameter downstream of the tube exit.
- CD as liquid velocity increases over a first threshold, drops with different masses detach in a chaotic manner, instability waves are observed from the tube exit, and the detachment point moves downstream to a few diameters from tube exit.
- J as liquid velocity increases further, the detachment point moves suddenly to a downstream distance of greater than 10 diameters, and a smooth jet is formed upstream of the break point.

In the current present CLSVOF calculation of this problem, the tube diameter was $D = 1.2$ mm. The fluid properties were: water with a density of 1000 kg/m^3 and a dynamic viscosity of 0.001 $Pa \cdot s$, air with a density of 1.205 kg/m^3 and a dynamic viscosity of $1.836 \times 10^{-5} Pa \cdot s$, and a surface tension coefficient of 0.0728 N/m. A Cartesian grid with a cell size Δ of 0.06 mm and a domain size $[0\ 60] \times [-2.5\ 2.5] \times [-2.5\ 2.5]$ mm were used with the tube exit centre located at (0, 0, 0). A uniform laminar flow was specified at tube exit. Simulations were carried out for three different liquid velocities 0.348 m/s, 0.434 m/s, 0.632 m/s, corresponding to jet Reynolds numbers of 415, 517, 755; these conditions were chosen to lie in PD, CD and J regimes respectively. Fig. 8 shows that periodic dripping, chaotic dripping and jetting modes were indeed predicted respectively at these three velocities. These results indicate that the transition from dripping to jetting was correctly predicted by the present two-phase LES formulation.

The liquid jet breakup length was computed for the jetting mode in two further simulations for liquid velocities equal to 0.817 m/s and 0.999 m/s. Since the three cases at the higher exit velocities are all in the jetting regime, the breakup length should be proportional to the liquid velocity (see [78]), and Fig. 9 indicates this was correctly predicted.

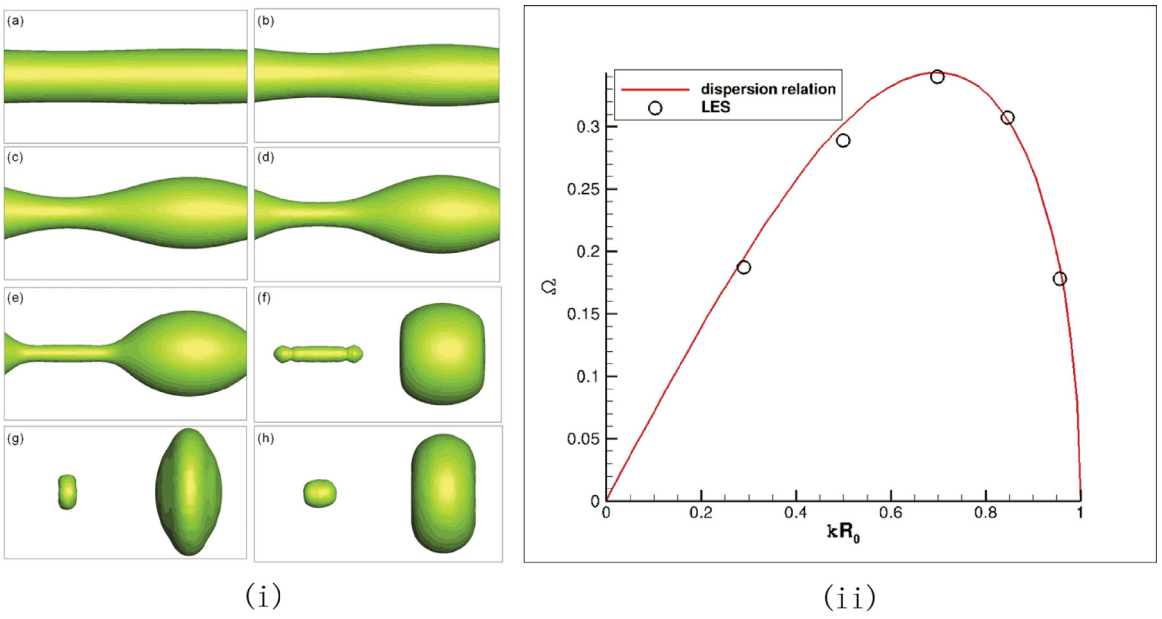

Fig. 7. (i): Plateau-Rayleigh deformation and breakup of liquid cylinder - $kR_0 = 0.698$ (a) t=5 s; (b) 40 s; (c) 55 s; (d) 60 s; (e) 65 s; (f) 70 s; (g) 75 s; (h) 80 s. (ii): Non-dimensional growth rate $\Omega = \omega\sqrt{\frac{\rho R_0^3}{\sigma}}$ vs perturbation wavenumber.

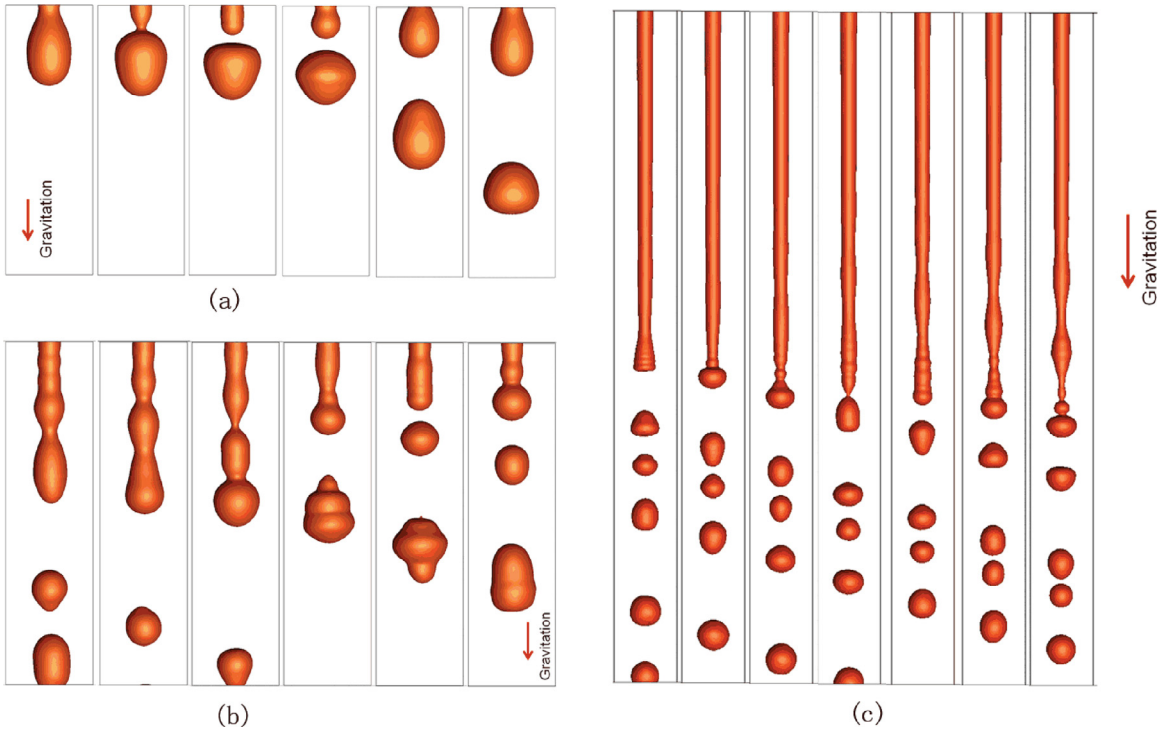

Fig. 8. Predicted (a) periodic dripping Re = 415; (b) chaotic dripping Re = 517; (c) jetting Re = 755.

4.4. Single water drop breakup in a uniform airstream

4.4.1. Resolution study

A water droplet in a uniform air flow is simulated for the temporal and spatial resolution study. The diameter of the initially spherical drop D_0 was 3.1 mm; the air density ρ_G and dynamic viscosity μ_G were $1.272 kg/m^3$ and $1.86 \times 10^{-5} Pa \cdot s$; the liquid density ρ_L and dynamic viscosity μ_L were $1002 kg/m^3$ and $0.892 \times 10^{-3} Pa \cdot s$ respectively; the surface tension coefficient σ was set to $0.072 N/m$. The air stream velocity is 15.7 m/s with a corresponding Weber number of 13.5. The corresponding Ohnesorge number ($Oh = \mu_L/\sqrt{\rho_L D_0 \sigma}$) is 1.9×10^{-3}. The simulation domain size is $[0\ 45.6] \times [-12\ 12] \times [-12\ 12]$ mm in the x, y, and z directions respectively. The centre of the initially static drop is located at (8, 0, 0) mm; in order to resolve the drop deformation and breakup process accurately, uniform cubic cells are used in the region $[0\ 40.8] \times [-5.1\ 5.1] \times [-5.1\ 5.1]$ mm with a cell size (δ) of 0.24 mm on Mesh M_0, 0.12 mm on Mesh M_1, $0.06\sqrt{2}$ mm on Mesh M_2, 0.06 mm on Mesh M_3, and 0.03 mm on Mesh M_4. In other regions of the simulation domain, a coarser mesh is used

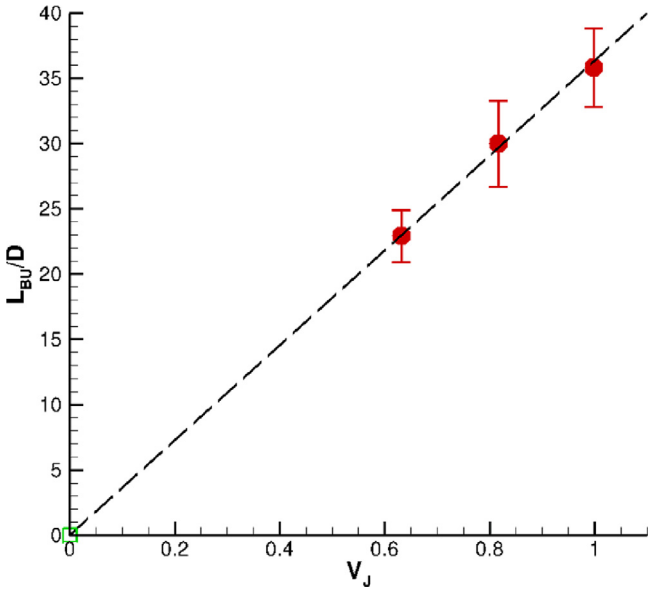

Fig. 9. Predicted breakup length vs liquid velocity in jetting regime.

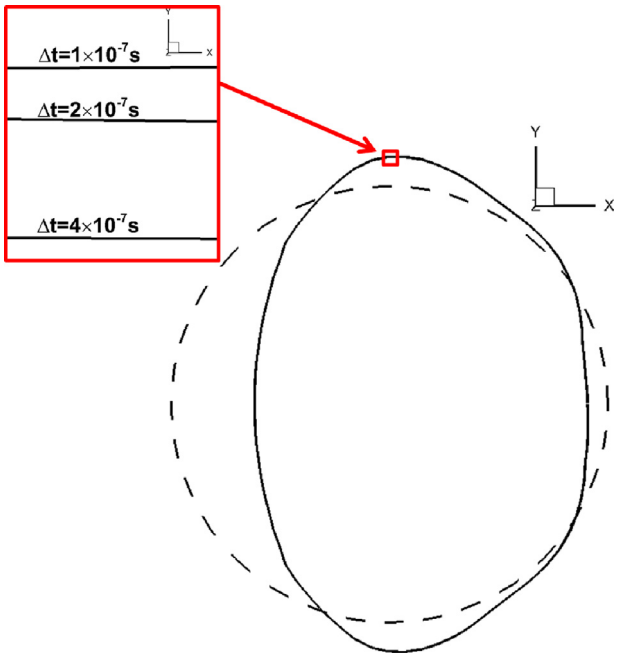

Fig. 10. Drop shape in plane z=0 at $T = 0.43$ predicted with different time steps (dashed line is the initial spherical drop).

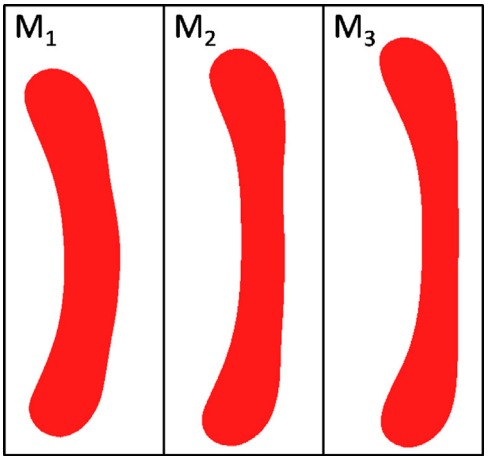

Fig. 11. Shape of predicted liquid disc at $T = 1.36$ on grids M_1, M_2, and M_3.

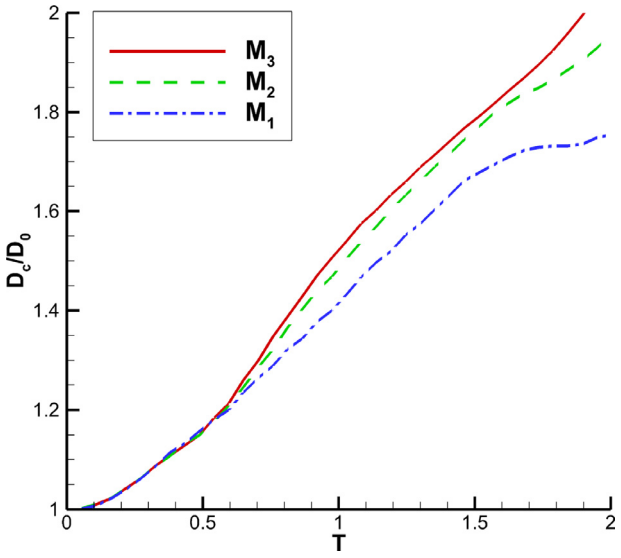

Fig. 12. Temporal growth of drop cross-stream dimension predicted by LES on three meshes.

to reduce the computational cost. In study of droplet deformation and breakup, a characteristic time scale is commonly defined as $t^* = \sqrt{\rho_L/\rho_G}\, D_0/U_G$ following [37,42]; the dimensionless time is then defined as $T = t/t^*$.

First, temporal resolution was investigated on mesh M_1. Three simulations were run with a time step of $1 \times 10^{-7}s$, $2 \times 10^{-7}s$, and $4 \times 10^{-7}s$, corresponding to a CFL number of ~ 0.025, ~ 0.05, and ~ 0.1 respectively. Fig. 10 shows the predicted shape of the deformed drop at $T = 0.43$ ($t = 2.4ms$). The predicted drop shapes in the three simulations effectively collapse onto each other. The predicted cross-stream diameter at this moment is measured in the zoomed-in view as shown in Fig. 10, resulting in 3.5156 mm, 3.5132 mm, and 3.508 mm. The cross-stream diameter difference between simulations with time steps of $2 \times 10^{-7}s$ and $4 \times 10^{-7}s$ is nearly twice that between simulations with time steps of $1 \times 10^{-7}s$ and $2 \times 10^{-7}s$, indicating that simulations with the current temporal discretisation scheme converge in first order as the time step decreases. This is reasonable since the first order forward Euler projection method was used. It is also observed that the cross-stream diameter difference between simulations with time steps of $1 \times 10^{-7}s$ and $4 \times 10^{-7}s$ is very small ($\sim 0.2\%$). Therefore, the time step corresponding to a CLF number of 0.1 was used in all following simulations.

In order to study the spatial resolution, simulations were carried out on meshes M_1, M_2, and M_3 respectively. Fig. 11 shows that the calculated drops deformed into the maximal liquid disc shape at $T = 1.36$ on meshes M_1, M_2, and M_3. This implies that the initiation time (period of the deformation stage) is predicted well on all three grids, although the cross-stream dimension of the liquid disc shows some difference. Fig. 12 shows the temporal growth of drop cross-stream dimension (D_c) predicted by LES on meshes M_1, M_2, and M_3. The difference of calculated D_c between meshes M_1 and M_2 is around twice that between meshes M_2 and M_3, implying that D_c converges in second order on mesh refinement.

Since the Rayleigh–Taylor instability (as the liquid drop is accelerated by the lighter gas) determines the drop breakup mode as detailed below, the drag which is correlated to the drop acceleration must be correctly reproduced in LES. Therefore, a convergence

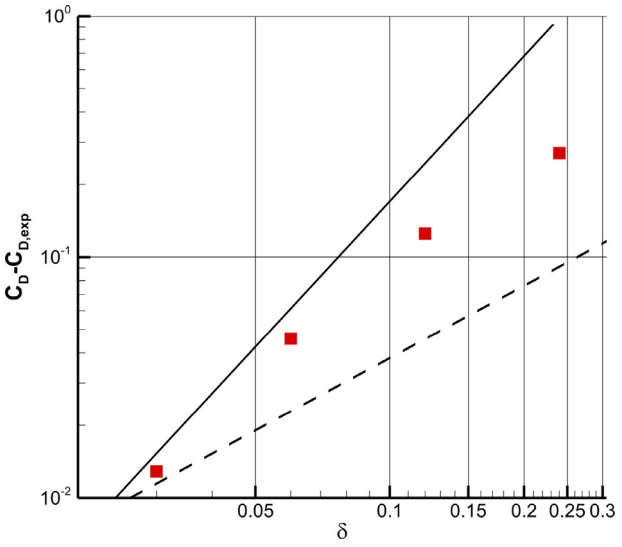

Fig. 13. Error in the predicted C_D vs the cell size δ. The solid and dashed lines are of slope 2 and 1 respectively.

study is carried out for the drag coefficient C_D which is related to the drag and the drop acceleration by:

$$C_D = \frac{F_D}{\frac{1}{2}\rho_G U_G^2 A} = \frac{ma}{\frac{1}{2}\rho_G U_G^2 A} = \frac{\rho_L \frac{\pi}{6} D_0^3 a}{\frac{1}{2}\rho_G U_G^2 \frac{\pi}{4} D_0^2} = \frac{4\rho_L D_0 a}{3\rho_G U_G^2} \tag{44}$$

where F_D is the drag, m is the drop mass, A and a is the cross section area and acceleration of the drop at the simulation initiation when the drop is still spherical. We first run the code by setting the velocity in the liquid to be 0 as if the drop is frozen until the gas flow around the drop fully developed. Then the two-phase simulation started running normally, and the drop acceleration at this moment is extracted from LES and used to calculate C_D. The experimental value for the drag of a solid sphere at the corresponding Reynolds number ($Re = \rho_G U_G D_0/\mu_G = 3328$) is $C_{D,\exp} = 0.39$ [79]. Four simulations were respectively run on grid M_0, M_1, M_3, and M_4. Fig. 13 shows the deviation of the predicted C_D from $C_{D,\exp}$ for increasing grid resolution. It is shown that C_D converges by around first order (from M_0 to M_1) at low grid grid resolution and by nearly second order (from M_3 to M_4) at high grid resolution.

4.4.2. Effect of Weber number

The effect of the Weber number on the breakup morphology is investigated here for a single water droplet in a uniform air flow, with the underlying physical mechanism examined. 3D illustrations of simulated oscillatory deformation ($We = 3.4$), bag breakup ($We = 13.5$) and sheet-thinning breakup ($We = 100$) have been presented in [69]. Four further simulations at Weber numbers of 12.5, 22, 25, 50 have been carried out here. The air stream velocities corresponding to the four Weber numbers are 15.1 m/s, 20 m/s, 21.3 m/s and 30.2 m/s. The physical properties of liquid and gas are the same as in subsection 4.4.1. The corresponding Ohnesorge number ($Oh = \mu_L/\sqrt{\rho_L D_0 \sigma}$) is 1.9×10^{-3}. All simulations were run on mesh M_3 detailed in subsection 4.4.1.

The simulated droplet undergoes bag breakup at $We = 12.5$ as for the case with $We = 13.5$. A bag-stamen breakup mode is predicted for the droplet at $We = 22$ and 25, with a 3D view of the breakup process illustrated in Fig. 14 for the case $We = 22$. As in bag breakup, the drop first deforms into a disc, with a noticeably larger dimension due to increased aerodynamic forces, see Figs. 14a-c. Fig. 14d indicates that the liquid film center is thick and a bag now grows between the rim and center. Eventually the bag bursts, leaving a liquid rim and a central liquid stamen (Fig. 14e-f).

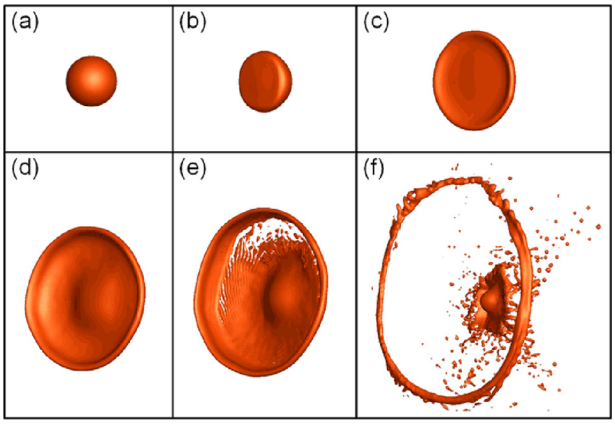

Fig. 14. 3D view of predicted bag-stamen breakup at We=22 (a) T=0.0 (b) 0.62 (c) 1.24 (d) 1.73 (e) 1.87 (f) 2.07.

Fig. 15 shows the predicted drop multimode breakup process for the case of $We = 50$. Figs. 15a-d illustrate that the drop first deforms into a staircase pyramid as observed in the experiments of Zhao et al. [41] [80]. Then the drop further deforms into a liquid disk (Fig. 15e), and a thin liquid sheet forms at the liquid disk periphery (Fig. 15f). Under the action of aerodynamic forces, thin liquid sheet is blown downstream (Fig. 15g), and the thin liquid film disintegrates (Fig. 15h), forming a large number of ligaments aligning to the air-stream direction (Fig. 15i). As the liquid ligaments disintegrates from the liquid disk, the centre part of the liquid disk evolves into a liquid core (Fig. 15j). The whole simulated multimode breakup process agrees well with the experimental observations for the case of $We = 49$ and $We = 53$ from Zhao et al. [41] [80].

According to experiments reported in [51] and [41], oscillatory deformation happens for $2.5 < We < 12$, bag breakup when $12 < We < 16$, bag-stamen breakup when $16 < We < 28$, multimode breakup when $41 < We < 80$, and sheet-thinning breakup when $We > 80$. For the Weber numbers chosen for the above test cases, the deformation/breakup morphology of the simulated droplet agrees well with experimental observations.

In order to explore further the mechanism of single drop deformation and breakup, a detailed analysis of velocity and pressure fields has been carried out. Fig. 16 shows predicted velocity vectors and pressure contours for We=13.5 at the early time of T=0.036, when the drop is still nearly spherical with only small induced liquid velocities. Similar to the flow around a solid sphere, the gas velocity reduces to zero at the front stagnation point, resulting in the highest gas phase pressure (Fig. 16a). The gaseous flow around the drop periphery accelerates, indicated by the low pressure zones. Vortices develop in the low pressure wake of the drop. The liquid velocity vectors and liquid in-plane streamtraces are visualised in Fig. 16b. Since the droplet is still nearly spherical, the liquid pressure on the interface is the sum of gas pressure and the almost constant pressure due to the jump arising from surface tension. Thus, the spatial pressure distribution within the liquid phase is directly determined by the gas pressure field. The pressure gradients inside the drop induce the liquid velocity, which moves liquid radially outward from front and rear stagnation regions to the drop periphery as indicated by the streamtraces.

Fig. 17 shows a similar picture as in Fig. 16b but now for the highest Weber number of 96, and at a later time of T=0.29 so that considerable drop shape distortion has occurred. On close examination, no evidence of any boundary layer can be seen in the liquid phase. This contradicts arguments previously put forward for the physical mechanism behind the shear-stripping mechanism,

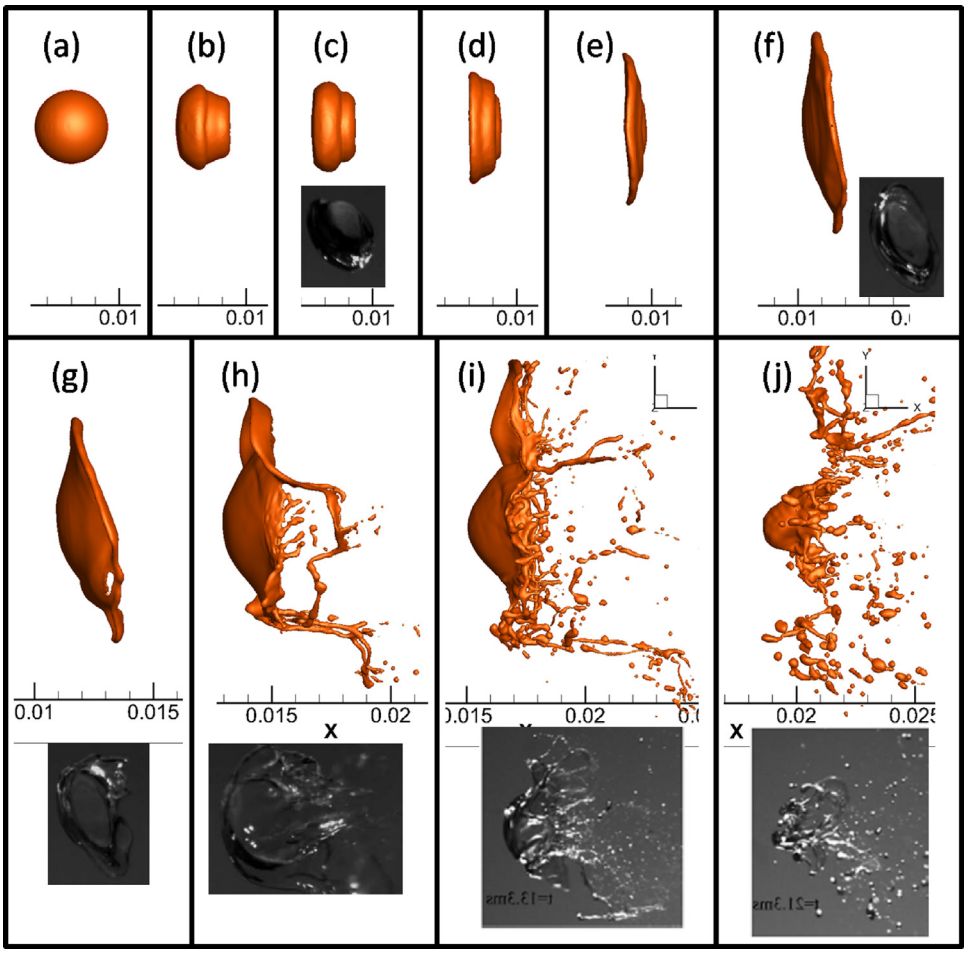

Fig. 15. 3D view of predicted multimode breakup at *We*=50 (a) T=0.07 (b) 0.42 (c) 0.56 (d) 0.76 (e) 0.98 (f) 1.25 (g) 1.39 (h) 1.67 (i) 1.87 (j) 2.15.(Photos in (c)(f)(g)(h) from [80] at *We*=49; photos in (i)(j) from [41] at*We*=53).

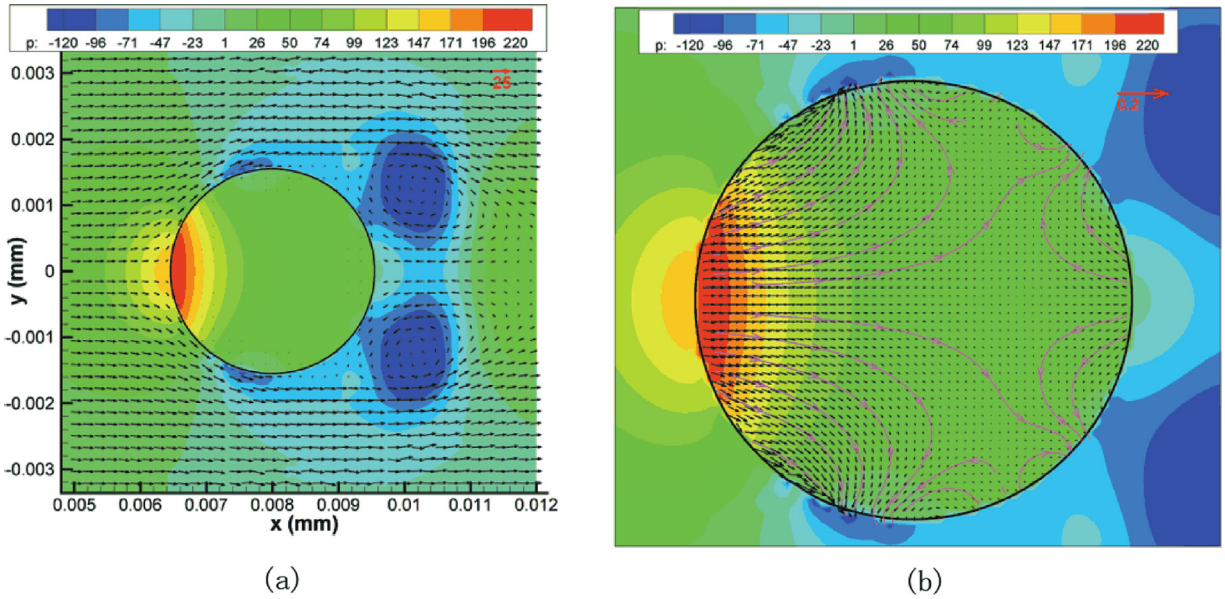

Fig. 16. Predicted velocity vectors and pressure contours at *T*=0.036 for *We*=13.5 (a) gas velocity vectors; (b) liquid velocity vectors and streamtraces (zoomed in view).

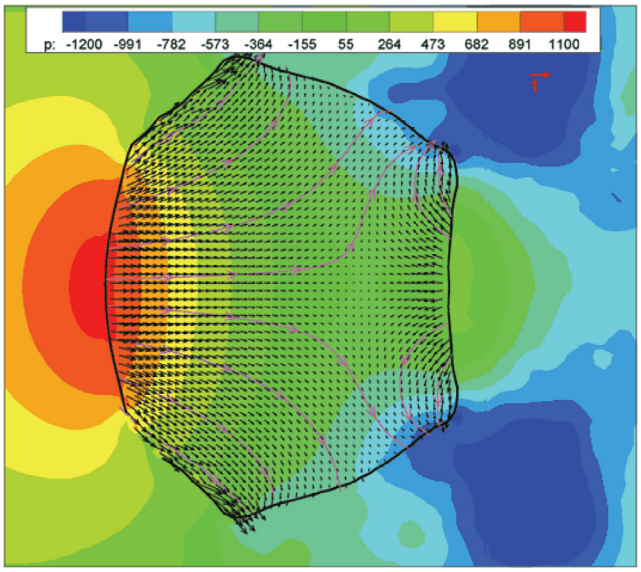

Fig. 17. Liquid velocity/streamtraces at T=0.29 for We=96.

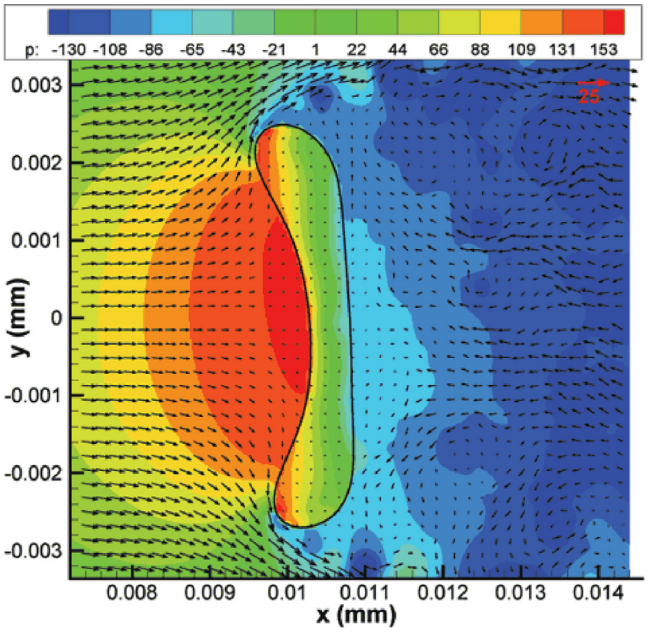

Fig. 18. Velocity and pressure fields at T=1.3 for We=13.5.

which postulated that a liquid boundary layer developed adjacent to the interface under the action of shear from the gas flow. The predicted liquid velocity vectors are effectively mainly controlled by the gaseous pressure distribution around the drop, with shear forces playing an insignificant role even at this high Weber number case.

Fig. 18 shows the velocity and pressure fields for the case We=13.5 at the later time of T=1.3 when the drop has deformed into a disc. Due to the large aerodynamically induced front/back pressure difference, the high-density liquid disc is accelerated considerably by the low-density air flow, resulting in a Rayleigh–Taylor (RT) instability [81,82]. At this Weber number, the RT wavelength is larger than the maximum cross stream diameter, producing a bag in the disc centre (Figs. 19d-e). As We increases to 22, the RT wavelength becomes shorter than the maximum cross stream diameter, resulting in a liquid disc with a greater thickness ventrally; the bag then forms between rim and thicker liquid centre

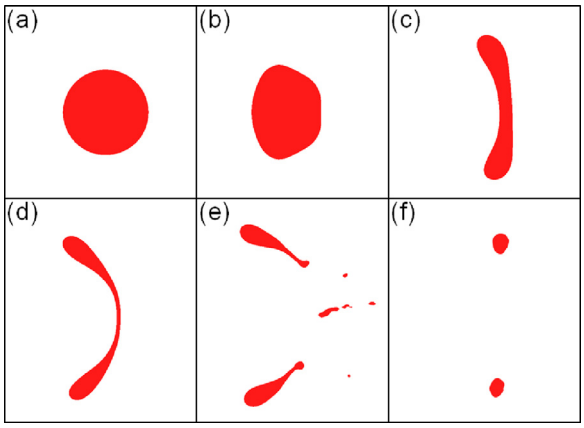

Fig. 19. 2D view (slice z=0) of predicted bag breakup We=13.5: (a) T=0.054 (b) 0.38 (c) 1.36 (d) 1.79 (e) 2.06 (f) 3.09 (scaled by 60%).

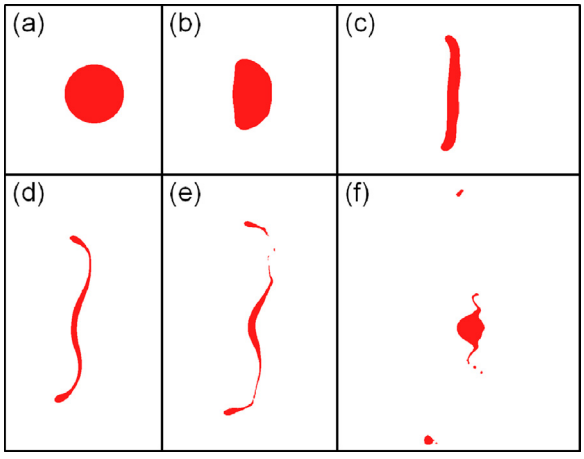

Fig. 20. 2D view (slice z=0) of predicted bag-stamen breakup We=22 (a) T=0.0 (b) 0.62 (c) 1.24 (d) 1.73 (e) 1.87 (f) 2.07.

(Figs. 20e-f). When We grows to 50, the periphery of the formed liquid disk is thinner than the disk center as shown in Fig. 21e, which is significantly different from the bag breakup mode (disk center is thinner than periphery as shown in fig. 19c) and bag-stamen breakup (disk center is nearly as thick as periphery as shown in Fig. 20c). The pressure contour lines in Fig. 22 show that the pressure gradient in the liquid disk periphery is higher than in the disk center. Therefore, the disk periphery is subject to stronger acceleration than the disk center, resulting in that the disk periphery bends downstream and the RT wave develops at the disk periphery as shown in Figs. 21f-g. As We increases further to 96, the RT wavelength decreases even more, and two waves of liquid films form and disintegrate sequentially from the main drop before leaving a central liquid core behind (Fig. 23). The rim of the RT wave becomes thinner and holds less mass due to its decreased wavelength as We increases; thus, when We=96, liquid wave rims are more prone to downstream deflection due to the smaller inertia of the rim liquid.

The droplet breakup process is divided into a deformation stage and a breakup stage. In the first stage, deformation into a liquid disc occurs under the pressure imbalance created by the gas flow. In the second, because the liquid disc is accelerated by the lighter gas phase, an RT instability is induced, forming a thin bag (bag or bag-stamen breakup) or a wave/ridge of liquid sheet (sheet-thinning breakup) on the drop periphery; it is these liquid structures which subsequently disintegrate into ligaments and droplets. The elapsed time of the deformation period (which ends when the

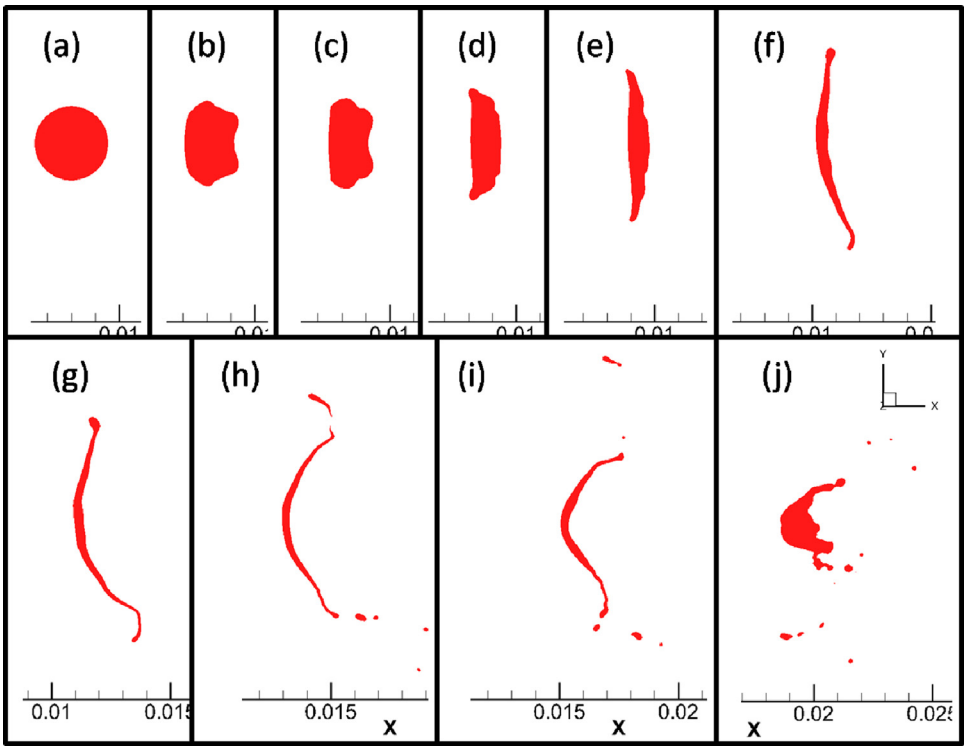

Fig. 21. 2D view (slice z=0) of predicted multimode breakup at *We*=50 (a) T=0.07 (b) 0.42 (c) 0.56 (d) 0.76 (e) 0.98 (f) 1.25 (g) 1.39 (h) 1.67 (i) 1.87 (j) 2.15.

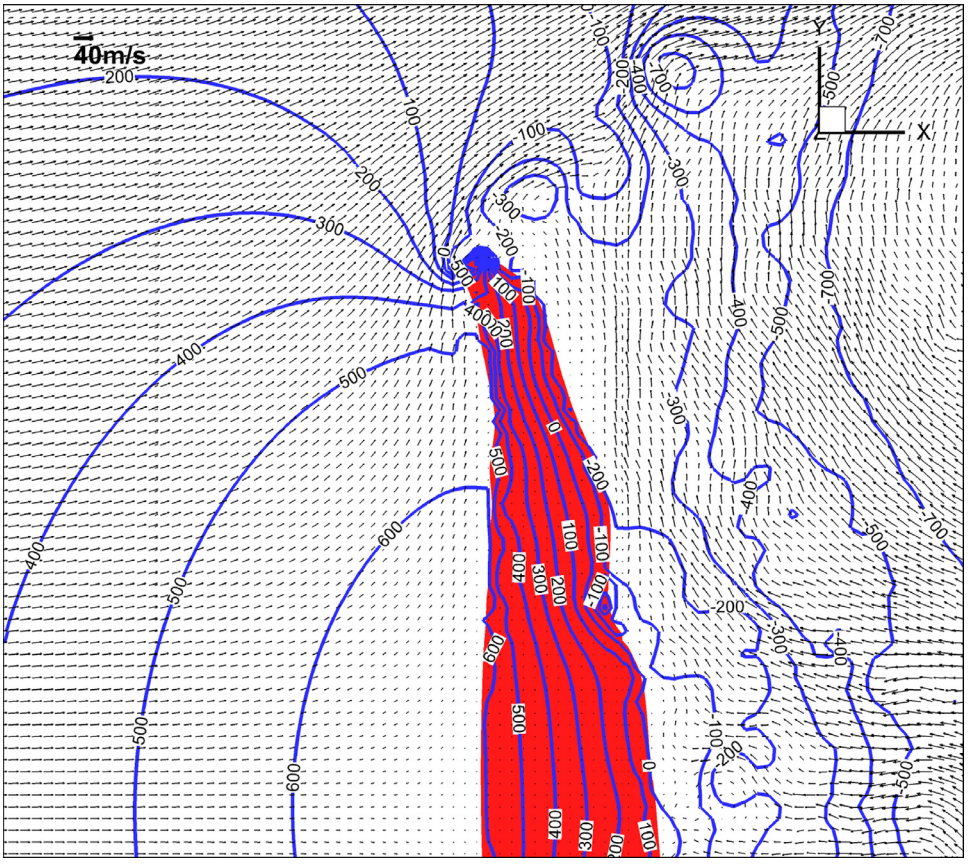

Fig. 22. The pressure contour lines in slice z=0 at T=0.98 at *We*=50.

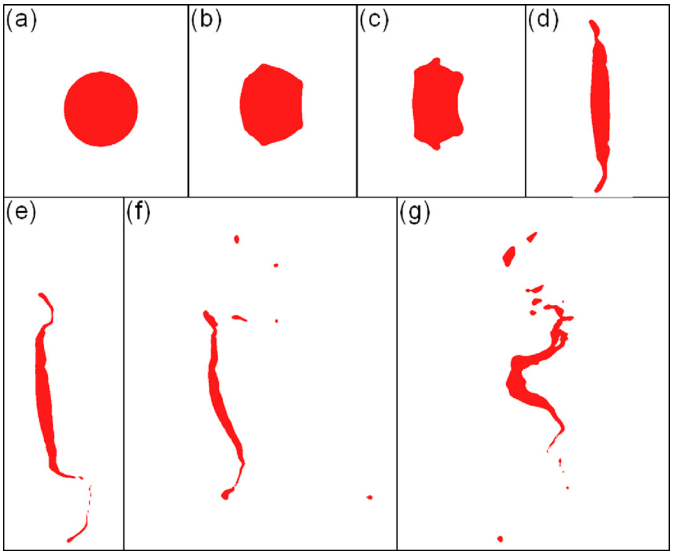

Fig. 23. 2D view (slice z=0) of predicted sheet-thinning breakup *We*=96 (a) T=0.096 (b) 0.29 (c) 0.48 (d) 0.96 (e) 1.15 (f) 1.44 (g) 1.83.

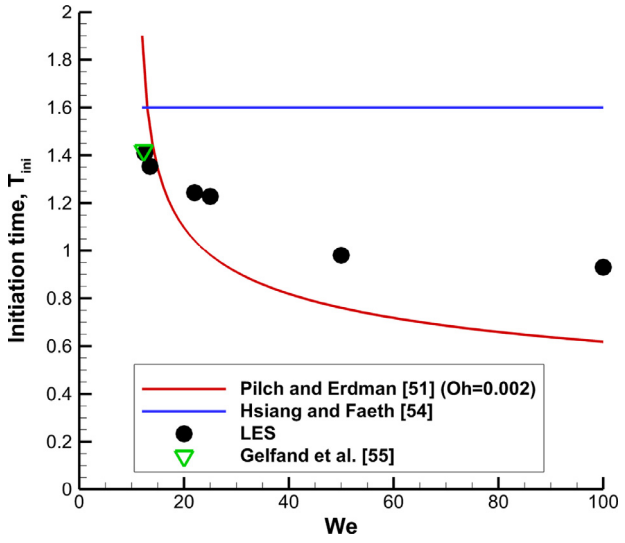

Fig. 24. Initiation time T_{ini} versus *We*.

disc reaches its maximum dimension) is defined as the breakup initiation time T_{ini}, and the disc diameter at this instant is defined as the maximum cross-stream dimension D_{max} as in [41]. Figs. 19a-c demonstrate that the liquid drop deforms into a liquid disc at the first three time snapshots whilst a bag can just be observed forming at the third. At T=1.36, the liquid disc reached its maximum cross-stream dimension $D_{max}/D_0 = 1.73$, and this is used to define the simulated initiation time. T_{ini} for a bag-stamen breakup mode is defined as the time instant shown in Fig. 20c; for multimode breakup, the initiation time is the moment when the drop evolves into a liquid disk as shown in Fig. 21e; for sheet-thinning breakup, the end of the deformation period is indicated in Fig. 23d.

Predicted initiation time T_{ini} and maximum cross-stream dimension D_{max} at different Weber numbers are compared with experiments in Figs. 24 and 25. Fig. 24 indicates that the deformation period calculated from the simulations reduces as *We* increases, which is consistent with the tendency observed by [51] in their review of available experiments. The predicted T_{ini} lies between Pilch and Erdman's data and Hsiang and Faeth's data [54] for *We* larger than $\sim$ 15. As the drop accelerates to the freestream velocity, the

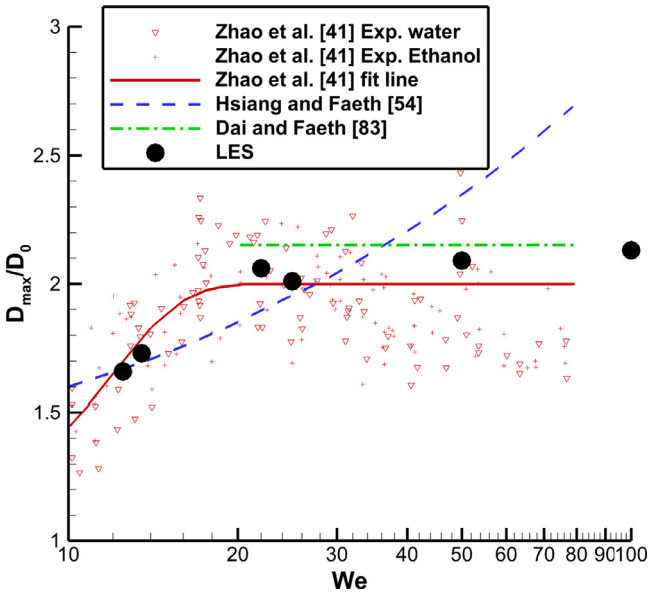

Fig. 25. Max cross-stream dimension D_{max} versus *We*.

aerodynamic force exerted on the drop is decreasing. The drop will either experience breakup in a finite time or only undergo deformation. Pilch and Erdman's data for Weber numbers approaching the critical value We_{cr} are doubtful since they imply infinite initiation time. [55] studied bag breakup at Weber numbers close to critical value in detail, and reported a non-dimensional initiation time of 1.42 at $Oh = 1.9 \times 10^{-3}$. T_{ini} predicted by the current methodology agrees well with this experimental result when *We* approaches the critical Weber number when breakup first begins We_{cr}. The predicted maximum cross-stream dimension at different Weber numbers obtained is presented in Fig. 25. Zhao et al.s experiments [41] found that D_{max} grows as *We* increases in the bag breakup regime, and this is reproduced well by the current algorithm. For bag-stamen and sheet-thinning breakup, the predicted D_{max} is approximately constant, located between the experiments of [41] and [83].

In order to calculate the RT instability wavelength, the acceleration of the drop is first computed as follows:

- The velocity of the centre of mass is computed from:

$$u_L = \frac{\sum_i u_i^L F_i \triangle_i}{\sum_i F_i \triangle_i}$$

  here $\triangle_i$ is the volume of cell i; u_i^L and F_i are the liquid velocity and VOF function in cell i respectively.
- The acceleration of the deformed drop is then calculated from

$$a_L = \frac{\mathrm{d}\, u_L}{\mathrm{d}\, t}$$

The acceleration of the drop over time is shown in Fig. 26, and the drag coefficient derived from the drop acceleration agrees well with the experimental measurements as shown in [26,69]. The acceleration is $230 m/s^2$ at the initiation time $T_{ini} = 1.36$ when the drop reaches its maximum cross stream dimension $D_{max} = 5.363 mm$. The wavelength of the most unstable RT wave is calculated from

$$\lambda_{max} = 2\pi \sqrt{\frac{3\sigma}{\rho_L a_L}} = 6.08 \text{ mm}$$

Following the definition in [41], the nondimensional RT wave number in the maximum cross stream dimension is computed as:

$$N_{RT} = \frac{D_{max}}{\lambda_{max}} = 0.88$$

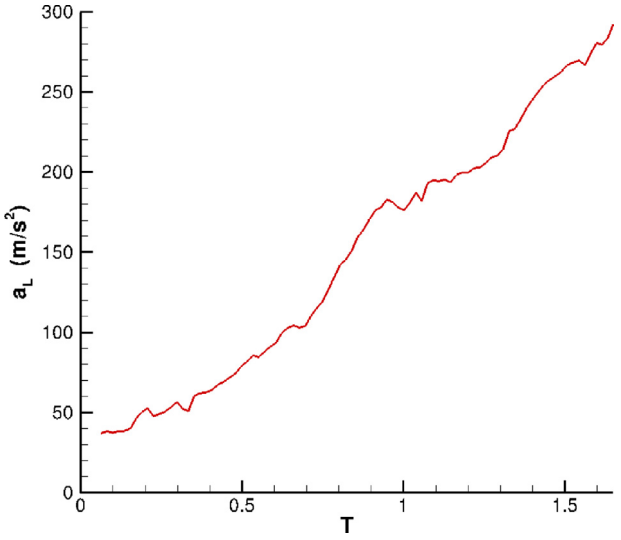

Fig. 26. Drop acceleration vs. time in a bag breakup (We=13.5).

For the bag-stamen breakup case ($We = 13.5$), $D_{max} = 6.4mm$, $\lambda_{max} = 4mm$, resulting in $N_{RT} = 1.6$. The simulation results therefore agree with Zhao et al.s experimental deduction [41] that bag breakup occurs when $1/\sqrt{3} < N_{RT} < 1$ and bag-stamen breakup when $1 < N_{RT} < 2$. This also confirms the descriptions provided above that it is a Rayleigh–Taylor instability that dominates the drop deformation and breakup process for the Weber number range studied.

4.4.3. Effect of Ohnesorge number ($Oh = \mu_L/\sqrt{\rho_L D_0 \sigma}$)

The present numerical methodology was used to investigate the effect of Oh on We_{cr}. Simulations were run at different Ohnesorge numbers by adjusting liquid viscosity. When water viscosity ($0.892 \times 10^{-3} Pa \cdot s$) was used as liquid viscosity as in the above subsections, $Oh = 1.9 \times 10^{-3}$. Simulations were run here for three Ohnesorge numbers 0.1, 0.7, and 2, by setting the liquid dynamic viscosity to $0.0473 Pa \cdot s$, $0.331 Pa \cdot s$, and $0.946 Pa \cdot s$ respectively. Since the drop breakup time grows as liquid viscosity increases, the breakup occurs further downstream. Thus, a simulation domain with a larger streamwise dimension than used above was needed. The domain size was altered to $[0\ 115.2] \times [-9\ 9] \times [-9\ 9]$ mm in the x, y, and z directions respectively. In order to reduce computational cost, a uniform fine mesh was used in the region $[0\ 115.2] \times [-4.8\ 4.8] \times [-4.8\ 4.8]$ mm with cell size 0.12 mm, and an expanding mesh was used elsewhere. Since the liquid flow inside the drop remains laminar in the drop deformation and breakup process, the computed SGS eddy viscosity must be small enough if it is not to interfere with the physical processes. Fig. 27 illustrates the computed Smagorinsky SGS eddy viscosity nondimensionalised by local gas/liquid molecular viscosity for the case with $Oh = 1.9 \times 10^{-3}$. In the gas phase, the SGS eddy viscosity took effect mainly in the wake region behind the drop and in the region adjacent to the interface to dissipate the smallest resolved eddy energy, ensuring the robustness of the proposed methodology. In the liquid phase, the SGS eddy viscosity was one order of magnitude smaller than the liquid molecular viscosity. At the low Oh of 1.9×10^{-3}, the liquid molecular viscosity will not influence the drop deformation/breakup, and this is also the case for the smaller SGS eddy viscosity in the liquid. As the liquid molecular viscosity grows to satisfy $Oh = 0.1$, the velocity gradient inside the drop decreases as shown in Fig. 28, and thus the computed SGS eddy viscosity declines in the liquid phase. Fig. 28 shows that the computed SGS eddy viscosity in the liquid was three orders of magnitude smaller than the high liquid molecular viscosity for the case with $Oh = 0.1$. For the two cases with $Oh = 0.7$ and $Oh = 2$, the non-dimensionalised SGS eddy viscosity in the liquid phase will be even smaller. Thus the effects of the liquid molecular viscosity on the drop deformation and breakup were correctly captured in the simulations without the pollution of SGS eddy viscosity.

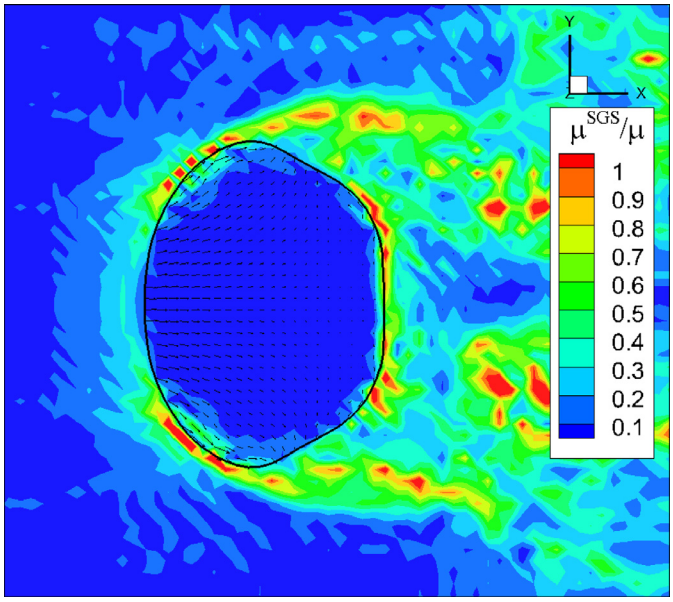

Fig. 27. SGS eddy viscosity (μ^{SGS}) nondimensionalised by local molecular viscosity (μ) in plane z=0 at $T = 0.36$ for $We = 13.5$ and $Oh = 1.9 \times 10^{-3}$.

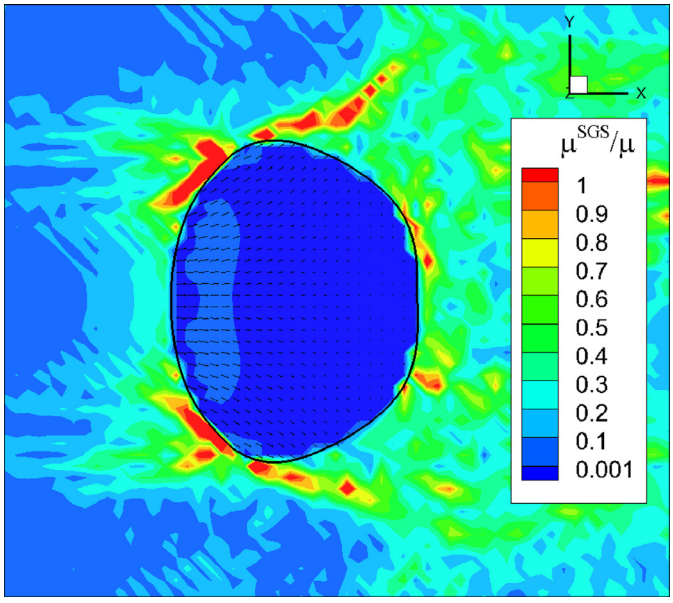

Fig. 28. SGS eddy viscosity (μ^{SGS}) nondimensionalised by local molecular viscosity (μ) in plane z=0 at $T = 0.36$ for $We = 13.5$ and $Oh = 0.1$.

Fig. 29 shows that two simulation cases were run for each Ohnesorge number: the first always displayed oscillatory deformation, and the second, at a slightly higher Weber number, displayed bag breakup. Based on these results, a line fitted between the simulations ($We_{cr} = 12.3(1 + 1.1\,Oh)$) agreed very well with the measurements of Lane [84], Hinze [85], Hanson et al. [86], Loparev [87], and Hsiang and Faeth [38], with the fitted correlation line matching Cohen's energy transfer analysis [53]. Finally, Fig. 30 shows the initiation time predicted in the four current LES

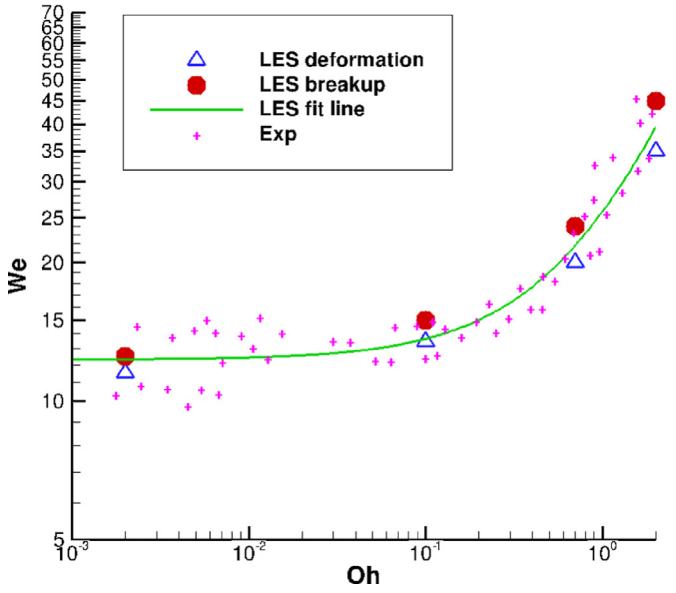

Fig. 29. Correlation between We_{cr} and *Oh*. Experimental Data extracted from Hsiang and Faeth [38].

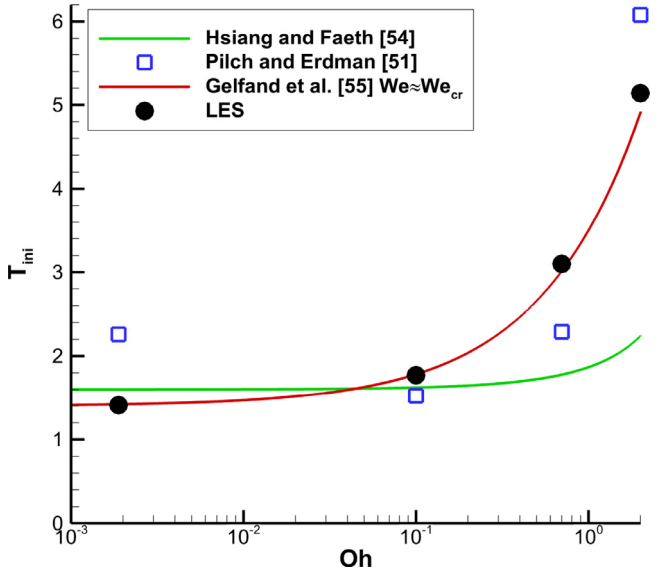

Fig. 30. Initiation time T_{ini} for different *Oh*.

breakup cases of Fig. 29. Pilch and Erdman [51], Hsiang and Faeth [54] and Gelfand et al. [55] have all proposed empirical correlations as shown in Fig. 30; the present results support Gelfand's correlation very closely since the data used by Gelfand were measured for bag breakup at approximately critical Weber numbers as is the case in the four simulations. These results confirm the accuracy of the present methodology for predicting We_{cr} and the effects of *Oh*.

5. Summary and conclusions

A quasi-DNS/LES algorithm for two-phase flows based on a CLSVOF formulation has been developed and applied in the present paper. Most importantly, the two-phase flow governing equations are discretised using an extrapolated liquid velocity approach, with sharp treatment of the density and molecular and SGS eddy viscosity. Several test cases were presented to demonstrate that the proposed method is accurate and robust, even at high liquid/gas density ratio. For the low-speed liquid jet, the transition from dripping to jetting mode is correctly predicted by the current two-phase flow solver. Simulations of breakup of a single drop showed that the breakup morphology can be correctly reproduced at corresponding *We* by the developed two-phase solver. The calculated velocity and pressure fields indicates that it is the Rayleigh–Taylor instability that determines the breakup mode in the studied *We* range, with the calculated Rayleigh–Taylor wavelength in good agreement with the experimental measurements. Finally, the effect of liquid viscosity on drop deformation and breakup is properly captured by the current simulations, showing that the critical Weber number required for breakup mode increases linearly with Ohnesorge number at high *Oh*. The initiation time characterising the start of droplet breakup is accurately predicted at different *We* and *Oh* numbers.

The present algorithm is developed for two-phase flow with high viscosity and density ratio where the velocity gradient in the liquid is much smaller than in the gas. For the two-phase flow with low viscosity and density ratio ($O(1)$) where the velocity gradient across the interface is in the same order of magnitude, considerable error will be introduced as the interface velocity is approximated by the neighbouring liquid velocity in the current method. Further work is required to develop a proper approximation to the interface velocity for all cases.

Acknowledgements

Financial support from EPSRC (SAMULET project and Dorothy Hodgkin Award (in conjunction with Rolls-Royce) for the first author) and National Natural Science Foundation of China (Grant No. 11402298) is gratefully acknowledged. The simulations were run on supercomputers Hydra of Loughborough University in UK and Tianhe-1A of National Supercomputing Center in Changsha in China.

References

[1] Gorokhovski M, Herrmann M. Modeling primary atomization. Annu Rev Fluid Mech 2008;40:343–66.
[2] Fuster D, Agbaglah G, Josserand C, Popinet S, Zaleski S. Numerical simulation of droplets, bubbles and waves: state of the art. Fluid Dyn Res 2009;41:065001.
[3] Hirt CW, Nichols BD. Volume of fluid method for the dynamics of free boundaries. J Comp Phys 1981;39:201–25.
[4] Rider WJ, Kothe DB. Reconstructing volume tracking. J Comp Phys 1998;141(2):112–52.
[5] Pilliod Jr JE, Puckett EG. Second-order accurate volume-of-fluid algorithms for tracking material interfaces. J Comp Phys 2004;199(2):465–502.
[6] Popinet S. An accurate adaptive solver for surface-tension-driven interfacial flows. J Comput Phys 2009;228:5838–66.
[7] Scardovelli R, Zaleski S. Direct numerical simulation of free-surface and interfacial flow. Annu Rev Fluid mech 1999;31:567–603.
[8] Scardovelli R, Zaleski S. Interface reconstruction with least-squares fit and split eulerian-lagrangian advection. Int J Numer Meth Fluids 2003;41:251–74.
[9] Gueyffier D, Li J, Nadim A, Scardovelli R, Zaleski S. Volume-of-fluid interface tracking with smoothed surface stress methods for three-dimensional flows. J Comp Phys 1999;152:423–56.
[10] Bianchi GM, Minelli F, Scardovelli R, Zaleski S. 3d large scale simulation of the high-speed liquid jet atomization. SAE tech pap 2007-01-0244 2007.
[11] Aulisa E, Manservisi S, Scardovelli R, Zaleski S. Interface reconstruction with least-squares fit and split advection in three-dimensional cartesian geometry. J Comput Phys 2007;225:2301–19.
[12] Fuster D, Bagué A, Boeck T, Moyne LL, Popinet LAS, et al. Simulation of primary atomization with an octree adaptive mesh refinement and VOF method. Int J Multiphase Flow 2009;35:550–65.
[13] Tomar G, Fuster D, Zaleski S, Popinet S. Multiscale simulations of primary atomization. Comput Fluids 2010;39:1864–74.
[14] López J, Hernández J, Gómez P, Faura F. A volume of fluid method based on multidimensional advection and spline interface reconstruction. J Comp Phys 2004;195(2):718–42.
[15] Sussman M, Smereka P, Osher S. A level set approach for computing solutions to incompressible two-phase flow. J Comp Phys 1994;114:146–59.
[16] Osher S, Fedkiw R. Level set methods and dynamic implicit surfaces. Springer-Verlag New York; 2003.
[17] Yue W, Lin CL, Patel VC. Numerical simulation of unsteady multidimensional free surface motions by level set method. Int J Numer Fluids 2003;42:853–84.

[18] Javierre E, Vuik C, Vermolen FJ, Segal A. A level set method for three dimensional vector stefan problems: dissolution of stoichiometric particles in multi–component alloys. J Comp Phys 2007;224(1):222–40.
[19] Pai MG, Desjardins O, Pitsch H. Detailed simulations of primary breakup of turbulent liquid jets in crossflow. In: Ann Res Briefs; 2008. p. 451–66.
[20] Herrmann M. A balanced force refined level set grid method for two-phase flows on unstructured flow solver grids. J Comp Phys 2008;227:2674–706.
[21] Lebas R, Ménard T, Beau PA, Berlemont A, Demoulin FX. Numerical simulation of primary break-up and atomization: dns and modelling study. Int J Multiphase Flow 2009;35:247–60.
[22] Desjardins O, Pitsch H. A spectrally refined interface approach for simulating multiphase flows. J Comp Phys 2009;228:1658–77.
[23] Sussman M, Puckett EG. A coupled level set and volume-of-fluid method for computing 3d and axisymmetric incompressible two-phase flows. J Comp Phys 2000;162:301–37.
[24] Sussman M, Smith KM, Hussaini MY, Ohta M, Zhi-Wei R. A sharp interface method for incompressible two-phase flows. J Comp Phys 2007;221:469–505.
[25] Ménard T, Tanguy S, Berlemont A. Coupling level set/VOF/ghost fluid methods: validation and application to 3d simulation of the primary break-up of a liquid jet. Int J Multiphase Flow 2007;33:510–24.
[26] Xiao F. Large eddy simulation of liquid jet primary breakup PhD thesis. Loughborough Univ.; 2012.
[27] Jalaal M, Mehravaran K. Transient growth of droplet instabilities in a stream. Phys Fluids 2014;26:012101.
[28] Rudmann M. A volume tracking method for incompressible multi-fluid flows with large density variations. Int J Numer Meth Fluids 1998;28:357–78.
[29] Raessi M. A level set based method for calculating flux densities in two-phase flows. Ann Res Briefs; 2008.
[30] Desjardins O, Moureau V. Methods for multiphase flows with high density ratio. Preceeding of the Summer Program; 2010.
[31] Toutant S, Chandesris M, Jamet D, Lebaigue O. Jump conditions for filtered quantities at an under-resolved discontinuous interface: Part 1 - theoretical development. Int J Multiphase Flow 2009;35:1100–18.
[32] Toutant S, Chandesris M, Jamet D, Lebaigue O. Jump conditions for filtered quantities at an under-resolved discontinuous interface: Part 2 - a-priori tests. Int J Multiphase Flow 2009;35:1119–29.
[33] Herrmann M, Gorokhovski M. A large eddy simulation subgrid model for turbulent phase interface dynamics. ICLASS 2009 Conf, Vail, Colorado USA; 2009.
[34] Herrmann M. A surface tension sub-grid model for phase interface dynamics. Proceeding Of Summer Program 2010, Centre for Turbulence Research, Stanford University, USA; 2010.
[35] Aniszewski W, Boguslawski A, Marek M, Tyliszczak A. A new approach to sub-grid scale surface tension for les of two-phase flows. J Comp Phys 2012;231:7368–97.
[36] Stolz S, Adams N, Kellar L. An approximate deconvolution model for large-eddy simulations with application to incompressible wall-bounded flows. Phys Fluids 2001;13:997–1015.
[37] Guildenbecher DR, López-Rivera C, Sojka PE. Secondary atomization. Exp Fluids 2009;46:371–402.
[38] Hsiang L-P, Faeth GM. Drop deformation and breakup due to shock wave and steady disturbances. Int J Multiphase Flow 1995;21:545–60.
[39] Theofanous TG, Li GJ, Dinh TN, Chang C-H. Aerobreakup in disturbed subsonic and supersonic flow fields. J Fluid Mech 2007;593:131–70.
[40] Theofanous TG, Li GJ, Dinh TN. Aerobreakup in rarefied supersonic gas flows. J Fluid Eng T ASME 2004;126:516–27.
[41] Zhao H, Liu H-F, Li W-F, Xu J-L. Morphological classification of low viscosity drop bag breakup in a continuous air jet stream. Phys Fluids 2010;22:114103.
[42] Ranger AA, Nicholls JA. Aerodynamic shattering of liquid drops. AIAA J 1969;7:285–90.
[43] Liu Z, Reitz RD. An analysis of the distortion and breakup mechanisms of high speed liquid drops. Int J Multiphase Flow 1997;23:631–50.
[44] Lee C, Reitz RD. An experimental study of the effect of gas density on the distortion and breakup mechanism of drops in high speed gas stream. Int J Multiphase Flow 2000;26:229–44.
[45] Theofanous TG. Aerobreakup of newtonian and vicoelastic liquids. Annu Rev Fluid Mech 2011;43:661–90.
[46] Han J, Tryggvason G. Secondary breakup of liquid drops in axisymmetric geometry. i. constant acceleration. Phys Fluids 1999;11:3650–67.
[47] Han J, Tryggvason G. Secondary breakup of liquid drops in axisymmetric geometry. ii. impulsive acceleration. Phys Fluids 2001;13:1554–65.
[48] Jalaal M, Mehravaran K. Fragmentation of falling liquid droplets in bag breakup mode. Int J Multiphase Flow 2012;47:115–32.
[49] Kkesi T, Amberg G, Wittberg LP. Drop deformation and breakup. Int J Multiphase Flow 2014;66:1–10.
[50] Brady P, Herrmann M, Lopez JM. Detailed numerical simulations of single drop atomization. In: ILASS-Americas 23rd Annual Conference on Liquid Atomization and Spray Systems, Ventura, CA; 2011.
[51] Pilch M, Erdman CA. Use of breakup time data and velocity history data to predict the maximum size of stable fragments for acceleration-induced breakup of a liquid drop. Int J Multiphase Flow 1987;13:741–57.
[52] Gelfand BE. Droplet breakup phenomena in flows with velocity lag. Prog Energ Combust 1996;22:201–65.
[53] Cohen RD. Effect of viscosity on drop breakup. Int J Multiphase Flow 1994;20:211–16.
[54] Hsiang L-P, Faeth GM. Near-limit drop deformation and secondary breakup. Int J Multiphase Flow 1992;18:635–52.
[55] Gelfand BE, Gubin SA, Kogarko SM, Komar SP. Singularities of the breakup of viscous liquid droplets in shock waves. J Eng Phys 1975;25:1140–2.
[56] Tang G, Yang Z, McGuirk JJ. Numerical methods for large-eddy simulation in general co-ordinates. Int J Numer Fluids 2004;46:1–18.
[57] Cheng L, Spencer A, McGuirk JJ. Comparison of unsteady reynolds averaged navier stokes and large eddy simulation cfd methodologies for air swirl fuel injectors. ASME J Eng Gas Turbines Power 2009;121:0115021.
[58] Cheng L, Dianat M, Spencer A, McGuirk JJ. Validation of les predictions of scalar mixing in high swirl fuel injector flows. Flow Turbul Combust 2012;88:146–68.
[59] Sagaut P. Large Eddy Simulation for incompressible flows. Springer; 2002.
[60] Pitsch H. A consistent level set formulation for large-eddy simulation of premixed turbulent combustion. Combust Flame 2005;143(4):587–98.
[61] Tryggvason G, Scardovelli R, Zaleski S. Direct numerical simulations of gas–liquid multiphase flows. Cambridge University Press; 2011.
[62] Prosperetti A, Tryggvason G. Computational methods for multiphase flow. Cambridge university press; 2009.
[63] Oberlack M, Wenzel H, Peters N. On symmetries and averaging of the g-equation for premixed combustion. Combust Theory Model 2001;5:363–83.
[64] Pitsch H. Large-eddy simulation of turbulent combustion. Annu Rev Fluid Mech 2006;38:453–82.
[65] Marmottant P, Villermaux E. On spray formation. J Fluid Mech 2004;498:73–111.
[66] Xiao F, Dianat M, McGuirk JJ. LES of turbulent liquid jet primary breakup in turbulent coaxial air flow. Int J Multiphase Flow 2014;60:103–18.
[67] Clanet C, Lasheras JC. Transition from dripping to jetting. J Fluid Mech 1999;383:307–26.
[68] Xiao F, Dianat M, McGuirk JJ. Large eddy simulation of liquid-jet primary breakup in air crossflow. AIAA J 2013;51:2878–93.
[69] Xiao F, Dianat M, McGuirk JJ. Large eddy simulation of single droplet and liquid jet primary breakup using a coupled level set/volume of fluid method. Atomization Spray 2014;24:281–302.
[70] Fedkiw R, Aslam T, Merriman B, Osher S. A non-oscillatory Eulerian approach to interfaces in multimaterial flows (the ghost fluid method). J Comp Phys 1999;152:457–92.
[71] Liu XD, Fedkiw R, Kang M. A boundary condition capturing method for Poisson's equation on irregular domains. J Comp Phys 2000;160:151–78.
[72] Kang M, Fedkiw R, Liu XD. A boundary condition capturing method for multiphase incompressible flow. J Sci Comput 2000;15:323–60.
[73] Dendy JE. Black box multigrid method. J Comp Phys 1982;48:366–86.
[74] Dendy JE. Two multigrid methods for three-dimensional equations with highly discontinuous coefficients. SIAM J Sci Stat Comput 1987;8:673–85.
[75] Moulton D., Berndt M., Dendy J.. https://software.lanl.gov/boxmg. 2010.
[76] MacLachlan SP, Tang JM, Vuik C. Fast and robust solvers for pressure correction in bubbly flow problems. J Comp Phys 2008;227:9742–61.
[77] Rayleigh L. On the instability of jets. Proc Lond Math Soc 1878;10:4–13.
[78] Dumouchel C. On the experimental investigation on primary atomization. Exp Fluids 2008;45:371–422.
[79] Munson BR, Young DF, Okiishi TH. Fundamentals of fluid mechanics. New York; 1990.
[80] Zhao H, Liu H-F, Xu J-L, Li W-F, Lin KF. Temporal properties of secondary drop breakup in the bag-stamen breakup regime. Phys Fluids 2013;25:054102.
[81] Rayleigh L. Investigation of the character of the equilibrium of ann incompressible heavy fluid of variable density. Proc Lond Math Soc 1882;14:170–7.
[82] Taylor GI. The instability of liquid surfaces when accelerated in a directon perpendicular to their planes. Proc Roy Soc A 1950;201:192–6.
[83] Dai Z, Faeth GM. Temporal properties of secondary drop breakup in the multimode breakup regime. Int J Multiphase Flow 2001;27:217–36.
[84] Lane WR. Shatter of drops in streams of air. Ind Eng Chem 1951;43:1312–17.
[85] Hinze JO. Fundamentals of the hydrodynamic mechanism of splitting in dispersion processes. AIChE Journal 1955;1:289–95.
[86] Hanson AR, Domich EG, Adams HS. Shock-tube investigation of the breakup of drops by air blasts. Phys Fluids 1963;6:1070–80.
[87] Loparev VP. Experimental investigation of the atomization of drops of liquid under conditions of a gradual rise of the external forces. Izvestiya Akad Nauk SSSR, Mekh Zhidkosti Gaza 3 1975:174–8.